CUSJ
COLUMBIA UNDERGRADUATE SCIENCE JOURNAL

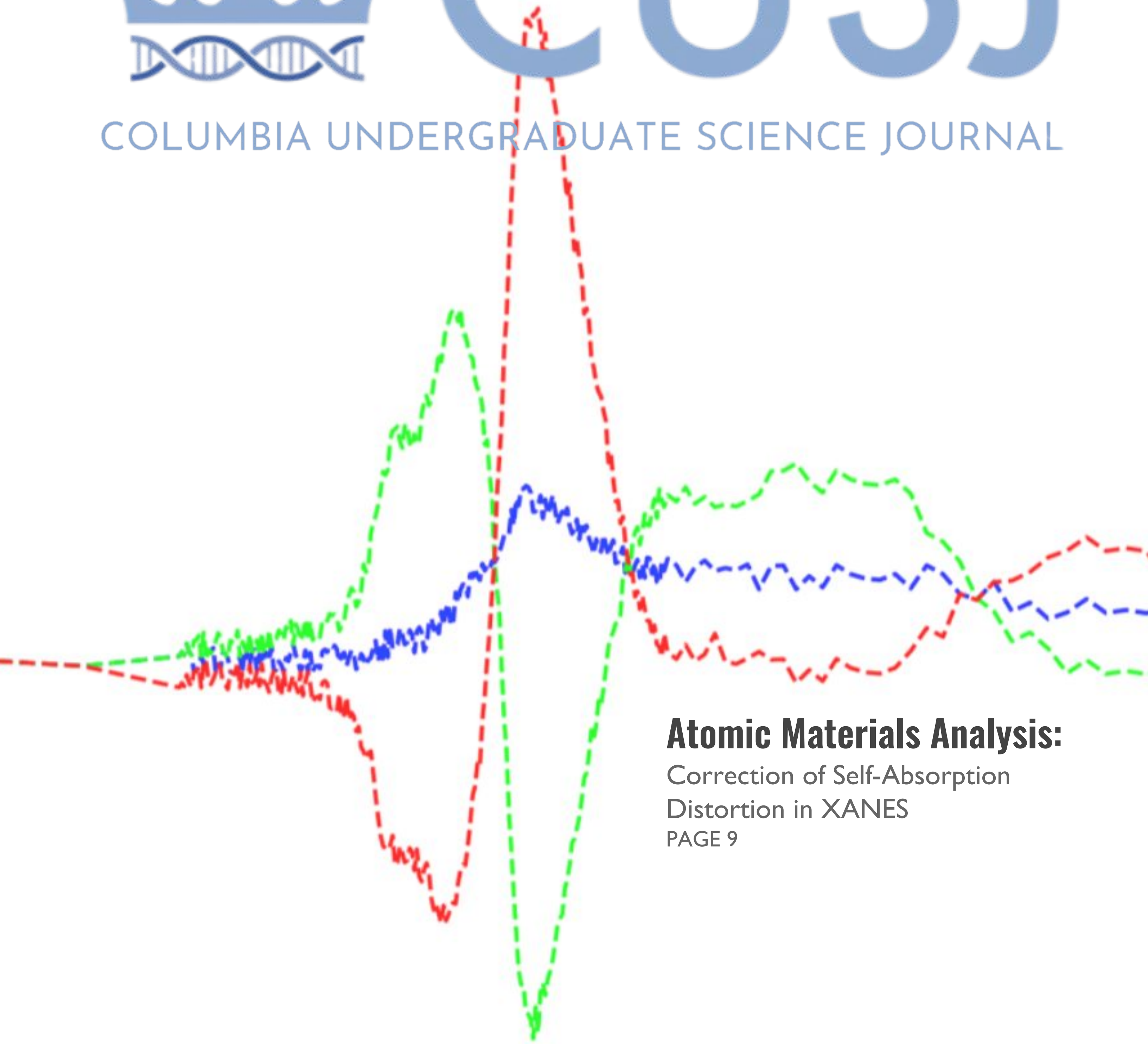

Atomic Materials Analysis:

Correction of Self-Absorption Distortion in XANES
PAGE 9

Volume 14 | 2020 | cusj.columbia.edu

CUSJ

Contents

Administration

Articles

Letter

Dear Readers,

It is with great excitement that I am able to present to you the CUSJ Volume 14 - 2020 Edition. Since our very first volume in 2006, it has been the mission of CUSJ to provide an accessible and professional, open access platform for undergraduates to communicate their research advances in various scientific fields. We CUSJ editors believe, as a community of young scientists and writers, that it is absolutely essential for researchers of all ages and levels of experience to have the opportunity to share their ideas and learn from their peers. Creating a space to facilitate that discussion is exactly what CUSJ aims to achieve not only with each volume, but also with our outreach to the public and numerous research oriented events.

COVID-19 has posed an incredibly difficult and tragic challenge to communities all over the world, scientists and non-scientists alike. With the shutdowns of universities accompanied by sudden changes in employment status and housing, the perseverance and determination shown by both our authors and editing team has been a true testament to their character, work ethic, and resilience. The hard work evident in each article of this volume, from experimental design to data interpretation, is a display of the talent and strength of our authors, and their ability to push on through an unprecedented global emergency. These undergraduates have shown that even during the most trying of times, while physically isolated, we can all still come together and communicate through science.

Volume 14 of CUSJ is diverse in scientific fields represented, ranging from biochemistry and the development of enzymatic nanoreactors for industrial synthesis, to the social science of shame in teens. Our cover features a graph from author Aidan Reddy’s cutting-edge investigation into X-ray absorption spectroscopy data processing, in which he develops a new method for spectra correction. His work should allow for more accurate analysis of various materials’ atomic properties, advancing the fields of both materials science and physics.

It has been a pleasure to serve as the Editor-In-Chief of CUSJ for the 2019-2020 academic year. My sincere thank you to everyone involved in the creation of this volume for their passion and commitment.

Julia Parsley
Editor-in-Chief

Letter

Dear Readers,

Founded in 2006, the *Columbia Undergraduate Science Journal* was created by a team of graduate students who wanted to provide a collegiate platform for undergraduates to publish their scholarship and to educate students about the academic publication process. With guidance from advisors and faculty, the editorial board strove to produce a professional-level, open-access science journal that provides participants with a valuable experience in publication. Since then our board has shifted to being solely composed of undergraduates. While still maintaining our core editorial standards, the journal has evolved to more explicitly try and foster a supportive student research community on our Morningside campus. It is this notion of community that can help us cope and process the unfamiliar circumstances of a global pandemic.

In quarantine, student researchers can reflect on the utility of science and its capacity to contain and eradicate this crisis. The collegiate scientists of today should recognize this moment for its affirmation in the power of collaboration and community. Recall this moment as you go onto make the next breakthroughs in the natural and applied sciences.

This year, the *Columbia Undergraduate Science Journal* formalized our intentions for community building, made inroads in connecting previous authors and alumni of our publication, and developed our editorial process further with open journal infrastructure. I was impressed by the quality of our submissions this year and I want to thank each of the authors for their cooperation in the compilation of our journal.

I am incredibly proud of what we have accomplished this year. Thank you all for your support in the growth of the student research community.

The *Columbia Undergraduate Science Journal* editorial board is proud to present the 14th annual *Columbia Undergraduate Science Journal*. Congratulations to the authors, thank you to our readers, and enjoy!

Sincerely,
Jason Mohabir
President CUSJ

CUSJ

People

Faculty Advisory Board

Hugh Ducklow	Professor of Earth and Environmental Sciences
Ivana Hughes	Director of Frontiers of Science, Senior Lecturer in Discipline - Chemistry
Marko Jovanovic	Professor of Biological Sciences
Laura Kaufman	Professor of Chemistry
Patricia Lindemann	Lecturer in Discipline and Director of Undergraduate Studies - Psychology
Kyle Mandli	Professor of Applied Mathematics
Matthew Palmer	Senior Lecturer and Director of Undergraduate Studies - E3B
Gerard Parkin	Professor of Chemistry
Ron Prywes	Professor of Biological Sciences
Angela Rasmussen	Associate Research Scientist - Center for Infection and Immunity

Editors

Julia Parsley	Editor-In-Chief, CUSJ
Kate Johnson	Editor-In-Chief, CJSJ
Jason Mohabir	President
Alex Ying	Director of Events
Arya Rao	Director of Internal Affairs
Ethan Chen	Director of Finance
Maria Trifas	Director of Outreach
Neeraj Sakhrani	Director of Communications
Ilaria Simeone	Editor
Vikas Chelur	Editor
Huck Jun Hong	Editor
Noah Krever	Editor
Elin Hu	Editor
Harrison Zhang	Editor
Elena Gribelyuk	Editor
Brendon Choy	Editor
Isabella Leite	Editor
Jacy Fang	Editor
Katie Long	Editor
Ashley Rosenberg	Editor
Sophia A Ladyzhets	Editor
Deena Shefter	Editor
Kanav Kalucha	Editor
Sahith Vadada	Editor
Lydia Wu	Editor
Arjun Kudinoor	Editor
Mayeesa Rahman	Editor
Aswath Suryanarayanan	Editor
Chloe Gong	Editor
Ellen Ren	Editor
Avi Gupta	Editor
Shivali Verma	Editor
Hibah Vora	Editor
Unal Yigit Ozulku	Editor
Michael Wang	Editor
Caroline Haoud	Editor
Shamara Yearwood	Editor

CUSJ

Article

Characterization & Correction of Self-Absorption Distortion in XANES

Aidan P. Reddy* and Apurva Mehta

SLAC National Accelerator Laboratory, 2575 Sand Hill Rd, Menlo Park, CA 94025*
***This is not the author's present address**

XANES, X-RAY ABSORPTION SPECTROSCOPY, NEAR EDGE STRUCTURE

ABSTRACT: X-ray absorption spectroscopy (XAS) is an experimental technique used to probe the atomic properties of materials. XAS measurements performed in fluorescence mode are subject to so-called "self-absorption" distortion, especially when the sample under investigation is thick or concentrated with respect to the atom of interest. Here we investigate the behavior of self-absorption and present several suggestions to avoid and manage self-absorption through experimental design. Particularly, we find that it is easier to correct for very thick samples than for samples of intermediate thickness. Self-absorption distortion necessitates a correction of the measured spectrum during data processing. We present a technique for correcting self-absorbed spectra in the XANES region that is effective for all sample thicknesses and experimental geometries.

INTRODUCTION

X-ray absorption spectroscopy (XAS) is a popular technique used to investigate the atomic properties of materials. XAS spectra indicate the absorption coefficient, μ_e(E), of a particular element and edge as a function of the energy of the incident X-ray. The structure of these spectra reveal electronic and geometric properties of a particular element within a sample. XAS spectra may be divided into two primary regions: X-ray absorption near-edge structure (XANES), which provides primarily electronic information (e.g. oxidation state), and X-ray absorption fine structure (XAFS), which provides primarily geometric information (e.g. coordination number).

XAS measurements are frequently taken in transmission mode, in which one compares the transmitted intensity and initial intensity of the X-ray beam to derive the absorption coefficient of the sample of interest μ_e(E), according to the relationship μ_t(E) = $-T \ln(\frac{I_0}{I})$, where T is the sample thickness, I_0 is the initial X-ray intensity, I is the intensity of the X-ray after traveling through the material, and μ_t(E) is the total absorption coefficient of the sample. The background component of μ_t(E), $\mu_b(E)$, which is the absorption coefficient due to elements and edges other than the one of interest, is subtracted from μ_t(E) to yield μ_e(E). μ_e(E) is then divided by $\mu_{e0+} \equiv \mu_e(E_{0+})$, where E_{0+} is an energy just above the edge, to obtain μ_n(E), the normalized version of $\mu_e(E)$.

Transmission mode measurements require that the sample absorb a significant portion of the intensity of the incident X-ray and thus that the sample be sufficiently thick (large T) or optically concentrated (large $\mu_t(E)$) [5]. Another common XAS technique which does not require these conditions is fluorescence mode. In fluorescence mode, one measures the fluorescence emitted from the sample as a result of the absorption of incident X-ray photons to infer μ_t(E). Fluorescence measurements, unlike transmission measurements, can be taken from more thin and optically dilute samples. In fluorescence mode, there is a linear relationship between the ratio of the measured fluorescence intensity to the incident X-ray intensity and the absorption coefficient of the target element and edge, $(I_f/I_0)(E) \propto \mu_e(E)$. However, this only holds when the sample under investigation is sufficiently thin or dilute with respect to the element of interest. For thicker and more concentrated samples, there is a nonlinear relationship between the fluorescence $\frac{I_f}{I_0}(E)$ and absorption $\mu_e(E)$ spectra, and their structures differ as a result. The variation between the fluorescence and absorption spectra that occurs for sufficiently thick samples is referred to as self-absorption. One should not read too much into this name. It is widely regarded as a misnomer, but nonetheless a well-established term.

It is possible to avoid self-absorption through experimental design, most straightforwardly through the choice or preparation of a sample that is sufficiently thin or dilute with respect to the element of interest. However, for various practical reasons, this is not always feasible. In this case, it is necessary to correct the measured fluorescence spectrum during the data-processing stage to reflect the structure of the desired spectrum, μ_n(E). A number of self-absorption correction algorithms have been presented in the past [1, 3, 7]. Various correction algorithms apply to different regions of the spectrum (XANES or XAFS), and each has its own limitations. For instance, a popular correction algorithm for the XANES region, FLUO, included in the popular XAS data processing program ATHENA, assumes that the relevant sample is at least a certain thickness, which we will discuss further. Thus, there remains a need for improved self-absorption correction methods with greater accuracy and wider applicability.

Here we will examine the dependence of self-absorption on various experimental parameters and provide experimental design suggestions for avoiding and controlling self-absorption. Additionally, we will present a correction method for the XANES region which may be applied to a range of sample thicknesses and experimental geometries. We will discuss its efficacy and limitations. The experimental data set used throughout is of a K_α emission line of a copper sample and was taken by Apurva Mehta and Ryan Davis.

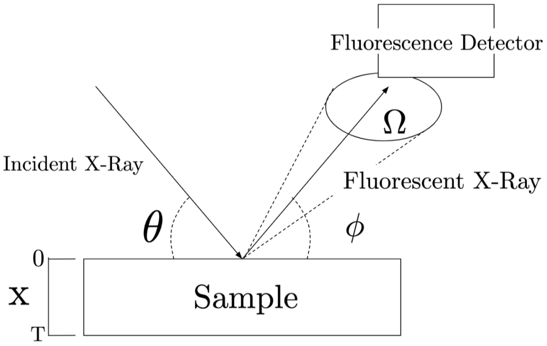

Figure 1. Schematic Diagram of Experiment. In standard geometry, $\theta = \pm = 45$. Even in nonstandard geometries, typically $\theta + \phi = 90$.

METHODS

Characterization of Self-Absorption

We begin with the fluorescence functional, a well-established equation that describes the ratio of fluorescence intensity to the intensity of the incident X-ray, $(I_f/I_0)(E)$, one would measure given an experimental geometry and chemical composition of a sample [4, 5]. The full derivation of this equation is given in appendix A.

$$\frac{I_f}{I_0} = (\frac{\Omega}{4\pi})\epsilon(E)\frac{\mu_e(E)}{\mu_t(E)+\mu_f\frac{\sin(\theta)}{\sin(\phi)}}\Big[1- e^{-(\mu_e(E)+\mu_b(E)+\mu_f\frac{\sin(\theta)}{\sin(\phi)})\frac{T}{\sin(\theta)}}\Big] \quad (1)$$

Here, $\mu_f \equiv \mu_t(E_f)$ is the total linear absorption coefficient at the fluorescence energy of the target edge (E_f). Generally, the linear absorption coefficient μ of an arbitrary material is given by $\mu = \sum_i \mu_{im}\rho_i$ where μ_{im} is the mass absorption coefficient and ρ_i is the density of a species we within the material. All other parameters are defined in the introduction or in Fig. I.

Just as $\mu_t(E)$ is background-subtracted and normalized to obtain $\mu_n(E)$, $\frac{I_f}{I_0}(E)$ is background-subtracted and normalized to obtain $(I_f/I_0)_N(E)$. In particular, a line is fitted to the pre-edge data to obtain $(I_f/I_0)_b(E)$, and this line is subtracted from the entire spectrum. Then the resultant spectrum is divided by $(I_f/I_0)_{0+} = (I_f/I_0)(E_{0+})$ to normalize. As is apparent in Fig. II(a), the thicker a sample is, the more self-absorbed its spectrum will be. We can define thickness more precisely in terms of attenuation length, defined as $l_{att} \equiv \frac{1}{\mu_t}$, or the depth within a sample at which the intensity of the incident X-ray will reach 1/e of its initial value. The attenuation length of copper at its K edge is $\approx 3.87\mu$m.

Qualitatively, self-absorbed $(I_f/I_0)_N(E)$ XANES spectra display enhanced pre-edge features and dampened post-edge oscillations (Fig. II(a)). The reason for this becomes apparent given a plot of the difference between a normalized absorption spectrum and fluorescence spectrum (Fig. II(b)). We see that there is an almost sinusoidal raising of values of the fluorescence spectrum compared to the absorption spectrum below $\mu_n = 1$ (corresponding to the edge and pre-edge, as well as troughs of the post-edge oscillations) and asymptotic lowering of values above $\mu_n = 1$ (corresponding to peaks of the post-edge oscillations).

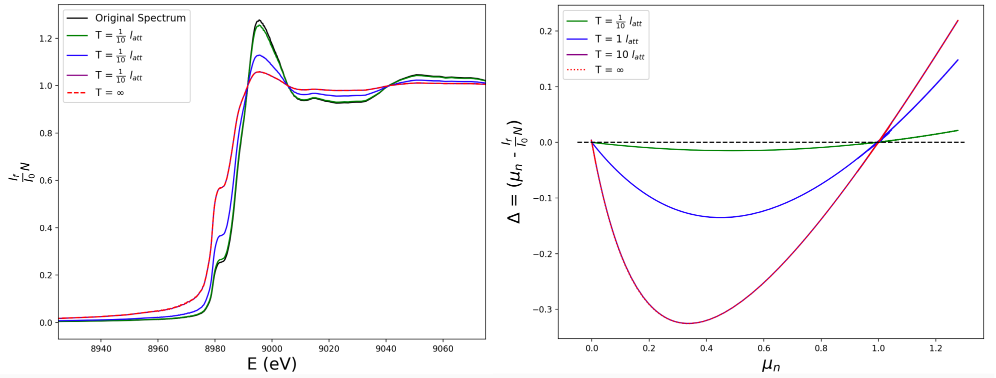

(a) **(b)**

Figure 2. Behavior of Self-Absorption Distortion for Various T. **a,** Simulated fluorescence spectra for various sample thicknesses compared to original, un-self-absorbed data of copper K edge. Self-absorbed spectra show increased values before and along the edge. The degree of self-absorption increases with thickness. however, $T = 10l_{att}$ yields a virtually identical spectrum to $T = \infty$. **b,** Difference between correct absorption coefficient, (μ_n), and simulated, normalized fluorescence spectrum, I_f/I_{0N}, as a function of μ_n for various thicknesses. Notice that the fluorescence spectrum is almost sinusoidally raised below the edge and at post-edge troughs, corresponding to $\mu_e(E) < \mu_{e0+}$, with the greatest decrease occurring around 1/3 of the way up the edge. Additionally, it is and more-or-less linearly increased for post-edge peaks, corresponding to $\mu_e(E) > \mu_{e0+}$. Lastly, note that, for thinner samples, self-absorption is most significant for post-edge peaks, and for thicker samples, self-absorption is most significant for the pre-edge and post-edge troughs.

By performing a first-order Taylor series approximation on the exponential term in (1), we find that $\frac{I_f}{I_0} \propto \mu_e$(E) when the quantity $[(\mu_t(E) + \mu_f\frac{\sin(\theta)}{\sin(\phi)})\frac{T}{\sin(\theta)}] << 1$, corresponding physically to very thin (small L) or optically dilute (small μ_t) samples.

$$\begin{aligned} &1 - e^{-(\mu_t(E)+\mu_f\frac{\sin(\theta)}{\sin(\phi)})\frac{T}{\sin(\theta)}} \\ &\approx 1 - (1 - (\mu_t(E) + \mu_f\frac{\sin(\theta)}{\sin(\phi)})\frac{T}{\sin(\theta)}) \\ &= (\mu_t(E) + \mu_f\frac{\sin(\theta)}{\sin(\phi)})\frac{T}{\sin(\theta)} \qquad (2) \end{aligned}$$

$$\begin{aligned} &\frac{I_f}{I_0} \\ &= (\frac{\Omega}{4\pi})\epsilon(E)\frac{\mu_e(E)}{\mu_t(E)+\mu_f\frac{\sin(\theta)}{\sin(\phi)}}((\mu_t(E)+\mu_f\frac{\sin(\theta)}{\sin(\phi)})\frac{T}{\sin(\theta)}) \\ &= (\frac{\Omega}{4\pi})\epsilon(E)\frac{T}{\sin(\theta)}\mu_e(E) \\ &\Rightarrow \frac{I_f}{I_0} \propto \mu_e(E) \qquad (3) \end{aligned}$$

When this is the case, the normalized fluorescence spectrum is the same as the normalized absorption spectrum: there is no self-absorption. however, when the sample is not very thin or dilute, this first-order approximation no longer holds, and, as is apparent from (1), the relationship between μ_e and I_f/I_0 becomes more complicated. In order for this first-order approximation to be valid, the sample must be extremely thin. A sample even 0.1 l_{att} can exhibit significant self-absorption (see Fig. II). In fact, we can predict the degree of self-absorption distortion that a given experimental spectrum will display. We can define the degree of self-absorption distortion as the difference between a normalized, background-subtracted, correct absorption spectrum, μ_n, and a normalized, background subtracted, self-absorbed fluorescence spectrum, $(I_f/I_0)_N$, and call this difference SAD. In order to do so, we will take advantage of results used for the self-absorption correction discussed later on (see appendix B).

$$\text{SAD} = \mu_n[1 - \frac{(\mu_{e0+} + \beta)[1 - e^{-(\mu_n \mu_{e0+} + \beta)L}]}{(\mu_n \mu_{e0+} + \beta)[1 - e^{-(\mu_{e0+} + \beta)L}]}] \quad (4)$$

In order for SAD to be less than 0.01 throughout the whole spectrum of the copper sample used in this work, corresponding to distortion of less than 1% where the percentage is relative to 1 on the normalized spectrum, T would need to be 0.18μm, or less than 4.7% of an attenuation length. This example demonstrates that the importance of diligent sample preparation to avoid self-absorption cannot be understated. Unless the experimenter takes special care to prepare an exceptionally thin sample, significant self-absorption distortion will occur. The equation for SAD (6), is not invertible in a closed algebraic form for L $\equiv T/\sin(\theta)$. however, one can easily evaluate the expression numerically to derive the maximum sample thickness that will keep SAD under a certain value, say 0.01. It is generally best to calculate SAD for highest the value of the normalized correct absorption spectrum, μ_n, one would expect to find, which corresponds to the highest peak in the μ_n spectrum. This is because, as demonstrated in Fig. II(b), self-absorption for thin samples is greatest at the highest value of the spectrum. Of course, an exact maximum value for μ_n cannot be known without an absorption spectrum to reference, but a reasonable guess can usually be made. For most absorption spectra, $\mu_{nmax} < 1.5$, so calculating SAD for μ_n = 1.5 will yield a value higher than one should actually encounter. however, for spectra with more exaggerated post-edge oscillations, calculating SAD for a larger value of μ_n will be necessary. For an index of the degree of self-absorption which is comparable from experiment to experiment, it may be useful to calculate SAD for a typical value of μ_{nmax}, say 1.2.

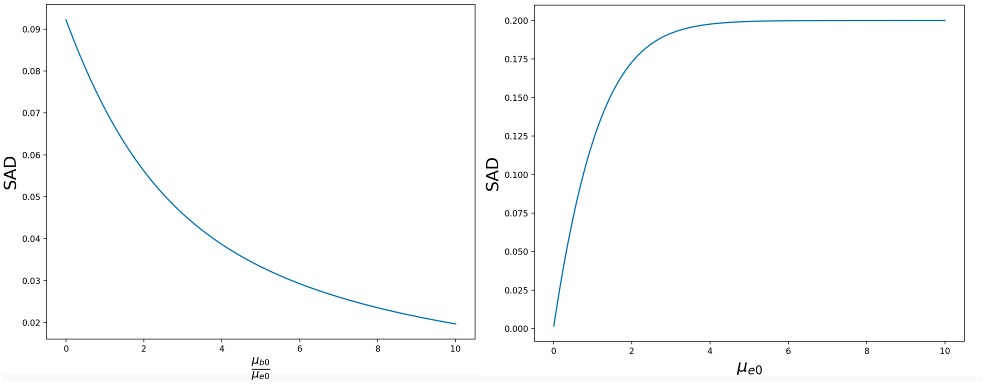

(a) **(b)**

Figure 3. Behavior of SAD. a, SAD as a function of μ_{b0}/μ_{e0} for T = 1/μ_{e0} (in other words, one attenuation length for the element of interest), μ_f = 0, and μ_n = 1.2. This demonstrates that, the larger the background absorption coefficient in proportion to that of the element and edge of interest, the less significant self-absorption distortion is. **b,** SAD as a function of μ_{e0} for T = 1, μ_f = 0, and μ_n = 1.2. This demonstrates that a greater concentration of the element of interest results in more significant self-absorption.

SAD provides another useful insight: by increasing $\mu_b(E)$, we can decrease SAD for a given $\mu_e(E)$ and T, as demonstrated in Fig. III. In other words, if we dilute the atom of interest in a dense matrix of heavier atoms (and maintain sample thickness), we can decrease the amount of self absorption. This effect is also apparent in (1). If μ_b(E) and μ_f are large, the variation in μ_e will result in relatively less change in the value of the exponential term. Additionally, variations in $\mu_e(E)$ will result in greater variations of the value of the fractional term as a whole, because the denominator will vary less. Physically, an increase in $\mu_b(E)$ will correspond to an increase in $\mu_f(E)$ because will be more and/or heavier atoms in the matrix, which will also absorb fluorescence photons. Thus, diluting the element of interest in a matrix of heavier atoms will decrease self-absorption even more than Fig. III(a) implies.

Conversely, self-absorption distortion will be most significant when $\mu_b(E)$ and $\mu_f(E)$ are minimized – that is, when the sample is concentrated with the element of interest. If we assume that our sample is very concentrated with the element of interest and thus $\mu_b(E) = \mu_f = 0$, then, in order for SAD ≤ 0.01 for μ_n = 1.2, T must be less than 0.085 $l_{att} \approx (1/12)l_{att}$. If μ_n = 1.5, then T $< 0.27 l_{att}$. Because this maximum value of T required to avoid self-absorption varies significantly from case to case, there is no precise rule of thumb regarding the maximum thickness with which to prepare your sample. However, it is typically on the order of hundredths to tenths of an absorption length.

For thick samples, it is particularly advisable to avoid high concentration with respect to the element of interest because self-absorption can become very significant. Specifically,

$$\mu_f = 0, \mu_t(E) = \mu_e(E) \\ \Rightarrow I_f = I_0(\frac{\Omega}{4\pi})\epsilon(E)[1 - e^{-\mu_t(E)\frac{T}{\sin(\theta)}}] \quad (5)$$

If the sample is very thick, the exponential term will approach zero and the fluorescence spectrum will exhibit minimal structure, making correction quite difficult. The lower $\mu_b(E)$ is in relation to $\mu_e(E)$, the higher the previously-discussed cap on self-absorption distortion in the thick limit becomes.

The greater the thickness of our sample is, the less accurate the first-order approximation (4) becomes, and thus self-absorption distortion increases. However, according to the fluorescence equation, there is a maximum amount of self absorption that can occur due to sample thickness. This is illustrated in Fig. II(b). The reason for this is that, for sufficiently large T, we may approximate the fluorescence equation to satisfy the T $\rightarrow \infty$ limit, yielding a much simpler and algebraically-invertible equation [5].

$$\lim_{T\rightarrow\infty}\Bigg(I_f = \\ I_0(\frac{\Omega}{4\pi})\epsilon(E)\frac{\mu_e(E)}{\mu_t(E) + \mu_f\frac{\sin(\theta)}{\sin(\phi)}}[1 - e^{-(\mu_t(E)+\mu_f\frac{\sin(\theta)}{\sin(\phi)})\frac{T}{\sin(\theta)}}]\Bigg) \\ = I_0(\frac{\Omega}{4\pi})\epsilon(E)\frac{\mu_e(E)}{\mu_t(E) + \mu_f\frac{\sin(\theta)}{\sin(\phi)}} \quad (6)$$

The percent error of the $T \rightarrow \infty$ approximation for a particular experiment is simply the magnitude of the exponential term in (1). Temporarily neglecting μ_f and assuming standard geometry ($\theta = \phi$ = 45º), it will take a sample of approximately $(-\ln(0.01)/\sin(45) \approx 3.3)l_{att}$ for the $T \rightarrow \infty$ to be accurate within 1%. However, if we attempt to apply a correction to this spectrum assuming that the $T \rightarrow \infty$ limit is satisfied, our corrected spectrum may be "overcorrected" more severely than 1%. Thus, as a general rule of thumb for standard geometry, it is advisable to ensure a sample thickness of $\leq (-\ln(0.001)/\sin(45) \approx 4.9)l_{att}$ before assuming the $T \rightarrow \infty$ limit. Additionally, as we have seen, significant self-absorption may occur even for a sample with a thickness on the order of microns. One must have more precise knowledge of a thin sample's thickness to properly correct for self-absorption — another reason to intentionally satisfy the $T \rightarrow \infty$ through the choice of a thick sample.

This provides a useful insight for experimental design: it is easier to correct a fluorescence spectrum taken from a sample of significant thickness than it is for a sample of intermediate thickness. One can use this equation as the basis for a straightforward correction algorithm. Daniel Haskel's FLUO, a popular self-absorption correction algorithm for XANES, does precisely that [3]. If a sample is very thick, one can use FLUO or the correction algorithm we will present to correct fluorescence spectra without precise knowledge of the sample's thickness. Thus, a very thick sample may be preferable to one of intermediate thickness, which will require the experimenter to have precise knowledge of its thickness in order to correct the spectrum accurately.

For thick samples, it is particularly advisable to avoid high concentration with respect to the element of interest, or, similarly, dilution in lighter elements. In this case, self-absorption can become very significant. In particular,

$$\Big(\mu_f = \mu_b(E) = 0\Big) \Rightarrow \frac{I_f}{I_0}_N = (\frac{\Omega}{4\pi})\epsilon(E)[1 - e^{-\mu_t(E)\frac{T}{\sin(\theta)}}] \quad (7)$$

If the sample is very thick, the exponential term will approach zero and the fluorescence spectrum will exhibit minimal structure, making correction quite difficult.

Additionally, as we decrease the incident angle θ, we increase the amount of self-absorption, as shown in Fig. VI. Intuitively, we can understand a decrease in incident angle as an increase in the effective thickness of the sample. In the case of normal incidence, grazing exit geometry (θ = 90º, ϕ = 0) we notice that I_f becomes proportional to μ(E), and thus there is no self absorption.

Assuming $\theta + \phi = 90^{\circ}$,

$$\lim_{\theta \to 90} \frac{I_f}{I_0} = (\frac{\Omega}{4\pi})\epsilon(E) \frac{\mu_e(E)}{\mu_e(E) + \mu_b(E) + \mu_f(\frac{\sin(90)}{\sin(0)} = \infty)} \Big[1 - e^{-(\mu_e(E) + \mu_b(E) + \mu_f(\frac{\sin(90)}{\sin(0)} = \infty))\frac{T}{\sin(0)}}\Big]$$
$$\Rightarrow (\frac{\Omega}{4\pi})\epsilon(E) \frac{\mu_e(E)}{\mu_e(E) + \mu_b(E) + \mu_f(\frac{\sin(90)}{\sin(0)} = \infty)} \propto \mu_e \tag{8}$$

Therefore, it is advisable to perform fluorescence measurements in this geometry if at all possible.

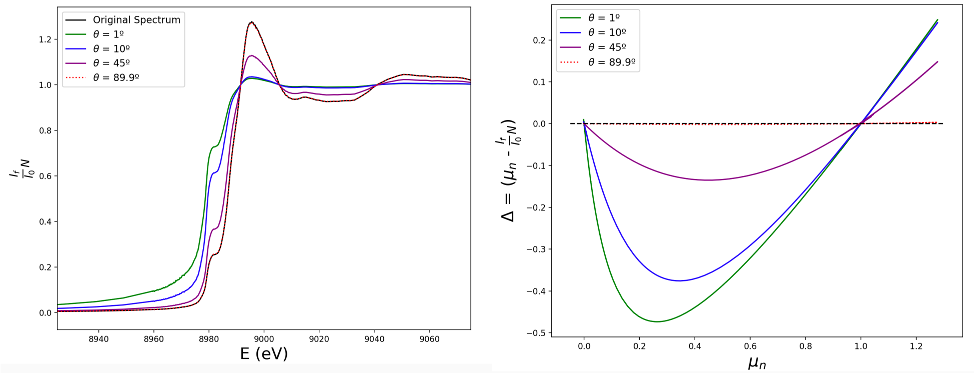

(a) **(b)**

Figure 4. Behavior of Self-Absorption Distortion For Various θ. a, Simulated fluorescence spectra for various incident angles compared to original, un-self-absorbed data of copper K edge, with the condition that $\theta + \phi = 90^{\circ}$. The degree of self absorption increases as θ decreases. Notice that for $\theta = 89.9$, there is virtually no self-absorption. **b,** Difference between correct and simulated spectra.

Self-Absorption Correction Derivation

The basis of this correction method is to use numerical calculation and tabulated data to work around the fact that the desired quantity, μ_e(E), may not be algebraically isolated in (1). We begin with a slightly reformulated fluorescence equation without constant multiplicative factors, which become unimportant upon normalization. We also make the approximation that $\epsilon(E)$ is constant over the XANES region, which is accurate because $\epsilon(E)$ does not vary significantly as a function of energy for a given chemical species.

$$\frac{I_f}{I_0}_N \propto \frac{\mu_e(E)}{\mu_t(E) + \mu_f g}[1 - e^{-(\mu_t(E) + \mu_f g)L}] \tag{9}$$

Here, $L \equiv T/\sin(\theta)$, $g \equiv \sin(\theta)/\sin(\phi)$. Taking tabulated data from [8], we may calculate:

$$\mu_f = \sum_i \mu_{m0i}(E_{0+})\rho_i \tag{10}$$

$$\mu_{b0} = \sum_i \mu_{m0i}(E_{preedge})\rho_i \tag{11}$$

$$\mu_{t0+} = \sum_i \mu_{m0i}(E_{0+})\rho_i \tag{12}$$

where we is an element within the sample.

$\mu_n = \mu_e/\mu_{e0+}$ is the spectrum that this correction will ultimately derive. Recall, it is the normalized, background-subtracted, and corrected absorption spectrum. Unless there is another atom in the sample with an edge at an energy in the XANES energy region of the element under investigation (a scenario which should be avoided if at all possible), μ_b(E) will be nearly constant over the XANES region, and thus we can approximate $\mu_b(E) \approx \mu_{b0} = \mu_b(E_{beforeedge})$. we may then calculate $\mu_{e0+} = \mu_{t0+} - \mu_{b0}$. We may also define $\beta \equiv \mu_{b0+} + \mu_f g$. Additionally, we may drop the explicit (E) dependence of terms within the expression. Given these amendments, we have:

$$\frac{I_f}{I_0}_N \propto \frac{\mu_n \mu_{e0+}}{\mu_n \mu_{e0+} + \beta}[1 - e^{-(\mu_n \mu_{e0+} + \beta)L}] \tag{13}$$

To normalize, we evaluate the right hand side of the equation at $\mu_n = 1$, or, equivalently, $\mu_e = \mu_{e0+}$. We then divide this value by 1 and call it "N" for normalization factor. We then multiply the right hand side by N. At this point, we may set the right and left hand sides of the equation to be equal because they are both normalized.

$$N \equiv \frac{1}{\frac{\mu_{e0}}{\mu_{e0+} + \beta}[1 - e^{-(\mu_{e0+} + \beta)L}]} \tag{14}$$

$$\frac{I_f}{I_0}_N = \frac{N \mu_n \mu_{e0+}}{\mu_n + \beta}[1 - e^{-(\mu_n \mu_{e0+} + \beta)L}] \tag{15}$$

Next, we calculate $\frac{I_f}{I_0}_N(E)$ for a large number of values of the final, normalized absorption spectrum μ_n between -.5 and 2. This range should suffice for most spectra one could reasonably encounter, but, of course, the range may be easily adjusted for atypical spectra. We now have a map SAC: $\frac{I_f}{I_0}_N(E) \mapsto \mu_n(E)$, where SAC is an acronym for "self-absorption correction", which we can use to correct our self-absorbed spectrum. One may replace each data point in a self-absorbed spectrum, F(E), with the value of $\mu_n(E)$ which corresponds to the nearest value for F(E) in the set of values in the map SAC that has been calculated. The result is the corrected spectrum, μ_n(E). Put simply, this method works around the lack of closed-form invertibility of the fluorescence equation to find an (almost) exact inverse numerically using tabulated values and approximations which are typically very strong over the XANES region.

To test the effectiveness of this correction method, we applied it to data that we simulated using the fluorescence equation and python. In particular, we took $I_f/I_0(E)$ data collected by Ryan Davis and Apurva Mehta on the K_α emission line of a copper sample, assumed to not be self-absorbed. We fitted this data set to tabulated linear absorption coefficient data for copper from NIST [6]. We then used the resultant spectrum as $\mu_t(E)$ in the simulations. For the simulations, we obtained $\mu_b(E)$ through a pre-edge linear regression fit the the pre-edge data of the $\mu_t(E)$ curve. We calculated $\mu_e(E)$ using $\mu_e(E) = \mu_t(E) - \mu_b(E)$. We subtracted the background of the simulated by performing a linear regression fit on pre-edge data and subtracting this line from my entire data set. We then flattened my data by performing a linear regression fit on post-edge data and subtracting this line from data after the edge. A polynomial fit to post-edge data would be more suitable for spectra with less-linear post-edge structures. Lastly, we normalized by dividing the entire spectrum by $(I_f/I_{0)}0+$, the value at which the post-edge flattened (but not yet normalized) data converged. All data processing, simulations, and plotting in this work we re done using Python. A data-processing program such as SIXPACK or ATHENA could be used for these initial steps.

As exhibited in Fig. V and VI, the correction method works uniformly well across different values of T and θ. Additionally, it is generally robust against errors in user-determined values of T and θ. However, as θ increases, or T decreases, the correction becomes less robust against mismeasurements, and the user must know their values with greater accuracy to correct well. Fig. V and VI also show that the difference between original and corrected spectra is greatest at the rising edge feature ($\approx 8985eV$) and the first peak ($\approx 9000eV$), indicating that the correction is least effective in these regions of the spectrum.

We note that this correction is not applicable to the "grazing-incidence" regime, wherein $\theta \leq \theta_c$, where θ_c is the samples critical angle for total external reflection. In this regime, (1) no longer applies.

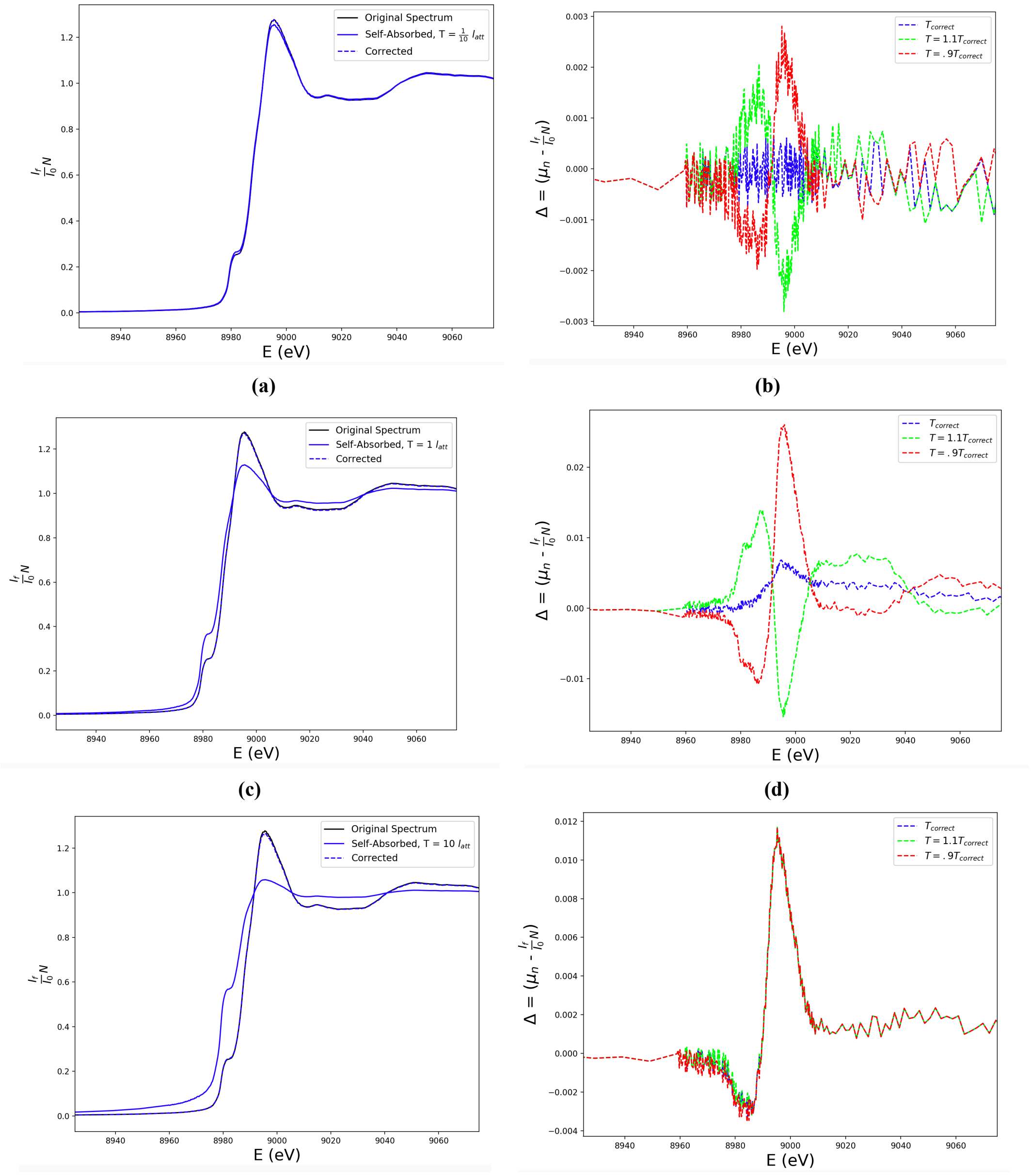

(a) **(b)**

(c) **(d)**

(e) **(f)**

Figure 5. Behavior of correction for various T. **a**,**c**, and **e** demonstrate the correction on simulated spectra of various thicknesses: T = $\frac{1}{10}$ l_{att}, T = $1l_{att}$, and T = $10l_{att}$ respectively. The original, un-self-absorbed spectra are compared to the simulated spectra for various T and the corrected versions of these simulated spectra. **b**, **d**, and **f** (corresponding to **a**, **c**, and **e**) show the difference between the original, un-self-absorbed spectra and the corrected spectra (in blue), as well as the differences between the original un-self-absorbed spectra and the corrected spectra, where the corrections are performed with incorrect sample thickness input, with +10% in green and -10% in red. This demonstrates the effectiveness of the correction and its robustness against mismeasured sample thicknesses (T).

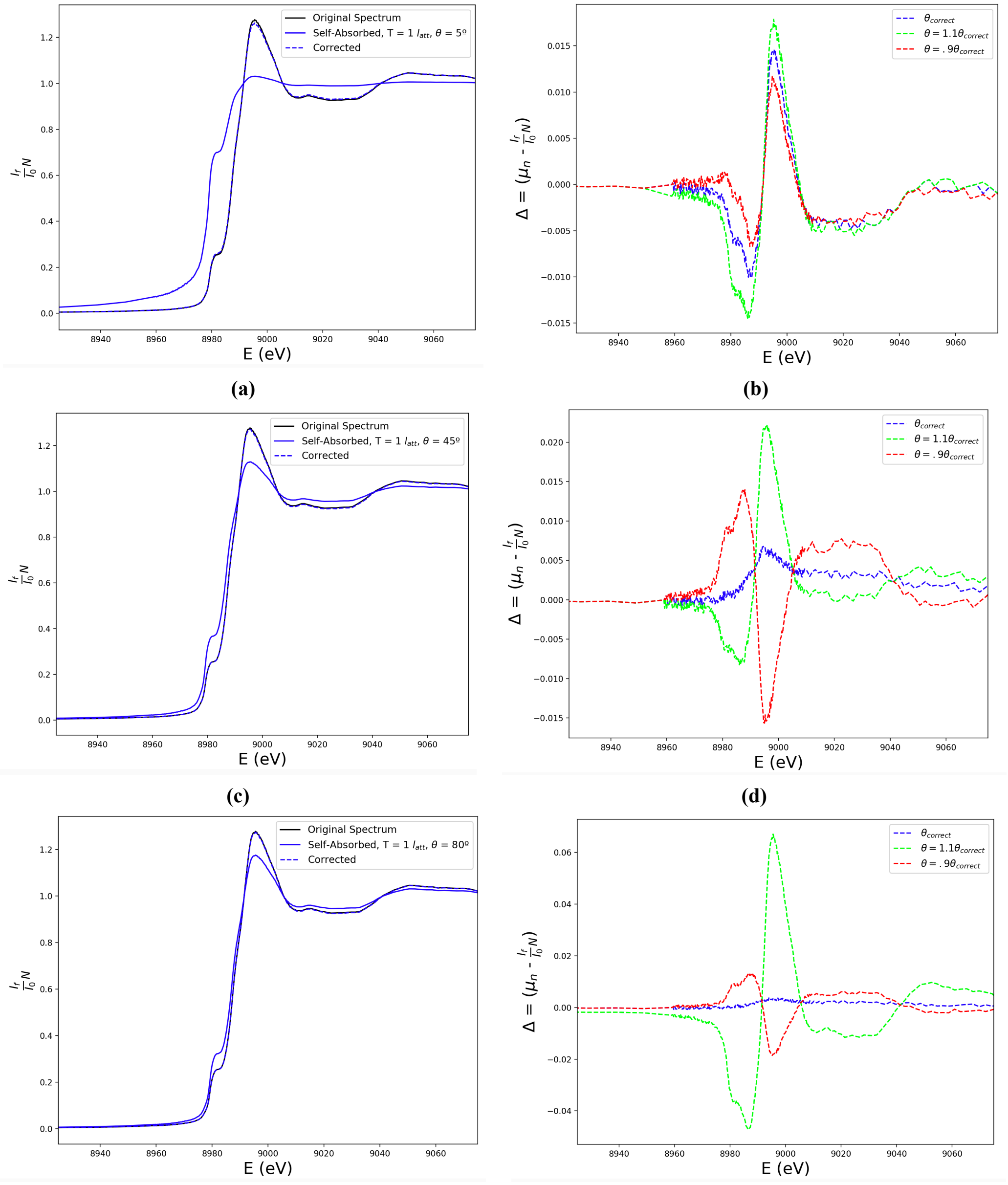

(a) (b)

(c) (d)

(e) (f)

Figure 6. Behavior of correction for various θ. **a**,**c**, and **e** demonstrate the correction on simulated spectra of various incident angles: $\theta = 5$º, $\theta = 45$º, and $\theta = 80$º respectively. The original, un-self-absorbed spectra are compared to the simulated spectra for various θ and the corrected versions of these simulated spectra. **b**, **d**, and **f** (corresponding to **a**,**c**, and **e**) show the difference between the original, un-self-absorbed spectra and the corrected spectra in blue, as well as the differences between the original, un-self-absorbed spectra and the corrected spectra, where the corrections are performed with incorrect θ, with +10% in green and -10% in red. This demonstrates the accuracy of the correction and its robustness against mismeasured θ.

DISCUSSION & CONCLUSION

We have investigated the behavior of self-absorption distortion. Additionally, we have gained a few insights which may be worth the consideration in designing a fluorescence-mode XAS experiment. Ideally, a sample will be sufficiently thin such that self-absorption distortion may be avoided altogether. We have demonstrated that this thinness is typically hundredths to tenths of an attenuation length. If obtaining this degree of thinness is not possible, it is preferable to choose a sample of $> 4.9l_{att}$ than it is to choose one of intermediate thickness. This is because, in order to correct a fluorescence spectrum measured from a sample of intermediate thickness, a more precise knowledge of T is required than is required to correct a spectrum from a sample of significant thickness. If it is known that the sample T is $> 4.9l_{att}$, no further knowledge of T is required to correct the spectrum accurately. The correction we have presented is based on the well-established fluorescence equation (2), and similar correction methods have been presented before, most notability by Iida and Noma [1]. however, this correction method is unique in that it takes in and puts out normalized, background-subtracted data. Additionally, it normalizes by μ_{e0+}, whereas Iida and Noma's correction normalizes by μ_{e0max} [1].

The correction method we present is strong, but there is room to incorporate more physical detail for improvement. For instance, it does not explicitly account fluorescence detector geometry and varying attenuation from pixel to pixel of the incident X-ray intensity on the path between the intensity monitor and the sample and as attenuation of the fluorescence X-ray intensity on the path from the sample to the fluorescence detector. however, this may be remedied, through the use of the SeAFFluX software package, which can adjust measured spectrum to account for these attenuation factors [7]. This adjusted spectrum can then be corrected using the method we have presented above. however, as Booth and Bridges noted in [2], the effect of integration of (2) over the solid angle of the detector is relatively insignificant in $\theta + \phi = 90$ geometries.

Although this correction method will not be perfect in all cases, we believe that there is little room for improvement beyond a correction which takes into account fluorescence detector geometry and beam attenuation from sources other than the sample as in SeAFFLuX, and then inverts (1) as in the correction method presented here [7]. Moving forward, there remains a need for a XANES correction in the grazing incidence regime.

AUTHOR INFORMATION

Corresponding Author

Aidan Reddy, Columbia University in the City of New York, NY, USA: aidan.reddy@columbia.edu

Funding Sources

This work was supported in part by the U.S. Department of Energy, Office of Science, Office of Workforce Development for Teachers and Scientists (WDTS) under the Science Undergraduate Laboratory Internships Program (SULI).

ACKNOWLEDGEMENTS

We thank Apurva Mehta and Ryan Davis for their support and guidance.

REFERENCES

[1] A. Iida, T. Noma, Correction of the Self-Absorption Effect in Fluorescence X-Ray Absorption Fine Structure. *Jpn. J Appl. Phys.* **32**, 2899-2902 (1993).

[2] C.H. Booth, F. Bridges, Improved Self-Absorption Correction for Fluorescence Measurements of Extended X-Ray Absorption Fine Structure. *Physica Scripta.* **T115** 202–204 (2005).

[3] D. Haskel, FLUO: Correcting XANES for Self-Absorption in Fluorescence Measurements. (1999).

[4] J. Goulon, C. Goulon-Ginet, R. Cortes, J.M. Dubois, On experimental attenuation factors of the amplitude of the EXAFS oscillations in absorption, reflectivity and luminescence measurements. *Journal de Physique.* **43 (3)**, 539-548 (1982).

[5] J. Jaklevic, J.A. Kirby, M.P. Klein and A.S. Robertson, G.S. Brown and P. Eisenberger,Fluorescence Detection of EXAFS: Sensitivity Enhancement for Dilute Species and Thin Films. *Solid State Communications* **23**, 679-682 (1977).

[6] National Institute for Standard and Technology, Physical Meas. Laboratory, Data from ”X-Ray Form Factor, Attenuation, and Scattering Tables. Available at https://physics.nist.gov/PhysRefData/FFast/html/form.html.

[7] R. M. Trevorah, C. T. Chantler, M. J. Schalken, Solving Self-Absorption in Fluorescence. *IUCrJ* **6**, 586-602 (2019).

[8] W.H. McMaster, N. Kerr Del Grande, J.H. Mallett, J.H. Hubbel. Compilation of X-Ray Cross Sections. Atomic Data and Nuclear Tables, **8**, 443-444 (1969).

APPENDIX A: DERIVATION OF FLUORESCENCE EQUATION

We begin with Beer's Law, which describes the exponential decay of the intensity of the incident X-ray as it travels through a sample as a result of absorption. See Fig. I for geometry.

$$\frac{dI(x)}{dx} = -I(x)\mu_t(E) \tag{16}$$

$$\int_0^{\frac{x}{sin(\theta)}} \frac{1}{I(x)} dI(x) = \int_0^{\frac{x}{sin(\theta)}} -\mu_t(E)dx \tag{17}$$

$$I(x) = I_0 e^{-\frac{\mu_t(E)x}{sin(\theta)}} \tag{18}$$

Here, I(x) is the intensity of the X-ray at a given depth; μ is the linear absorption coefficient, equivalent to $\sum_i \mu_i = \sum_i \mu_{mi}\rho_i$, where we is an element within the material, μ_{mi} is its mass absorption coefficient and ρ_i is the density of a the element within a material; and I_0 is the intensity of the X-ray prior to entering the material. The absorption of a photon does not necessarily result in the release of a fluorescence photon. For instance, it may result in the release of an Auger electron instead. The portion of absorption events resulting in fluorescence may be defined as $\epsilon(E)$, a function of energy. Intuitively, the total fluorescence, $I_{ftot}(x)$ must be equal to $I_{abs}(x)$, the total absorbed intensity multiplied by $\epsilon(E)$.

$$\begin{aligned} I_{ftot}(x) &= \epsilon(E) I_{abs} \\ &= \epsilon(E)(I_0 - I(x)) = \epsilon(E) I_0 (1 - e^{-\frac{\mu_t(E)x}{sin(\theta)}}) \\ \Rightarrow \frac{dI_{ftot}(x)}{dx} &= \epsilon(E) I_0 \frac{\mu_t(E)}{sin(\theta)} e^{-\frac{\mu_t(E)x}{sin(\theta)}} \end{aligned} \tag{19}$$

When a photon is released from an atom, it must travel through the bulk of the material before arriving at fluorescence detector. On this journey, fluorescence X-rays attenuate according to Beer's Law. Additionally, a given edge of a given atom will fluoresce photons of a characteristic energy, E_f = E_x - E_b, where E_x is the energy of the incoming X-ray photon and E_b is the binding energy of the absorbing electron. Fluorescence photons are emitted isotropically. A fluorescence detector does not entirely surround a material, so it does not detect all of the fluorescence emitted from the sample. Instead, it detects a portion of $\frac{\Omega}{4\pi}$ of all the fluorescence photons emitted, where Ω is the solid angle in steradians around the sample which the fluorescence detector covers. Taking this into account, we find:

$$\frac{dI_f(x)}{dx} = \frac{\Omega}{4\pi} \epsilon(E) I_0 \frac{\mu_t(E)}{sin(\theta)} e^{-\frac{\mu_t(E)x}{\sin(\theta)}} e^{-\frac{\mu_f x}{\sin(\phi)}} \tag{20}$$

Where I_f is the measured fluorescence intensity and μ_f = $\mu_t(E_f)$ is the total linear absorption coefficient at the energy of the fluorescence photons. A given edge of a given atom will fluoresce photons of a characteristic energy, E_f = E_x - E_b, where E_x is the energy of the incoming X-ray photon and E_b is the binding energy of the absorbing electron. We must now integrate over the entire depth of the material. Finally, we integrate over the entire depth of the material.

$$\int_0^T dI_f(x) = \int_0^T \frac{\Omega}{4\pi} \epsilon(E) I_0 \frac{\mu_t(E)}{\sin(\theta)} e^{-(\frac{\mu_t(E)}{\sin(\theta)} + \frac{\mu_f}{\sin(\phi)})x} dx \tag{21}$$

$$\begin{aligned} &I_f(T) - I_f(0) = I_f = \\ &\frac{\Omega}{4\pi} \epsilon(E) I_0 \frac{\mu_t(E)}{\sin(\theta)} \frac{1}{-(\frac{\mu_t(E)}{\sin(\theta)} + \frac{\mu_f}{\sin(\phi)})} [e^{-(\frac{\mu_t(E)}{\sin(\theta)} + \frac{\mu_f}{\sin(\phi)})T} - 1] \\ &\Rightarrow I_f = \frac{\Omega}{4\pi} \epsilon(E) I_0 \frac{\mu_t(E)}{\mu_t(E) + \mu_f \frac{\sin(\theta)}{\sin(\phi)}} [1 - e^{-(\mu_t(E) + \mu_f \frac{\sin(\theta)}{\sin(\phi)}) \frac{T}{\sin(\theta)}}] \end{aligned} \tag{22}$$

APPENDIX B: DERIVATION OF SAD

$$\text{SAD} \equiv \mu_n - \frac{I_f}{I_{0\;N}} \tag{23}$$

We then consider (15) and (16), yielding:

$$\begin{aligned} \frac{I_f}{I_{0\;N}} &= \frac{\frac{\mu_n \mu_{e0+}}{\mu_n \mu_{e0+} + \beta} [1 - e^{-(\mu_n \mu_{e0+} + \beta)L}]}{\frac{\mu_{e0+}}{\mu_{e0+} + \beta} [1 - e^{-(\mu_{e0+} + \beta)L}]} \\ &= \frac{(\mu_{e0+} + \beta)[1 - e^{-(\mu_n \mu_{e0+} + \beta)L}]}{(\mu_n \mu_{e0+} + \beta)[1 - e^{-(\mu_{e0+} + \beta)L}]} \\ \Rightarrow \text{SAD} &= \mu_n [1 - \frac{(\mu_{e0+} + \beta)[1 - e^{-(\mu_n \mu_{e0+} + \beta)L}]}{(\mu_n \mu_{e0+} + \beta)[1 - e^{-(\mu_{e0+} + \beta)L}]}] \end{aligned} \tag{24}$$

CUSJ Article

Protein-Polymer Complex Coacervates as Synthetic Membrane-less Organelles

Hansen Tjo[1]*, Nicholas Zervoudis[2], Allie C. Obermeyer[2]

[1]Department of Chemical Engineering, University of Massachusetts Amherst
[2]Department of Chemical Engineering, Columbia University in the City of New York

COMPLEX COACERVATION, PROTEIN ENGINEERING, SOFT MATTER

ABSTRACT: In solution, oppositely-charged macromolecules undergo charge-mediated liquid-liquid phase separation into a complex coacervate phase – a dense, macromolecule-rich liquid. In nature, the basis for intracellular compartmentalization in the formation of membrane-less organelles has been shown to follow similar complexation principles, where charged proteins represent the ionic species. We seek to capture the spatiotemporal tunability properties of such organelles for enzymatic reactions in vitro. However, the in vitro formation and deformation of protein-based coacervate microenvironments as a nanoreactor is a limiting factor. Here, we prescribe high-precision turbidimetry coupled with optical microscopy, to characterize the phase behavior of binary protein-polymer complexes between the weak anionic enzyme Glucose Oxidase (GOx) and four different synthetic polycations as functions of composition and ionic strength. Establishment of conditions ideal for coacervate formation in each protein-polymer system informed pH titration experiments on characterizing self-assembly regulation. The results from this study will help inform the design of novel coacervate microenvironments for industrial enzyme cascades and elucidate the role of associative phase separation in cellular evolution.

INTRODUCTION

Selectivity and specificity are an enzyme's key characteristics [1, 3, 4]. As biological catalysts, enzymes increase rates of reaction such that greater amounts of biological product may be obtained under less time. They also have been used to improve chemical processes in industries from food, agriculture, and petroleum in addition to reducing energy costs and operation time [4].

It is difficult to synthetically match the efficacy and specificity of enzymes as biochemical systems have had millions of years to evolve [4, 16]. While advents in directed evolution and protein engineering attempt to circumvent the time required for natural evolution, amongst other approaches to improve enzyme activity, there is also particular interest to achieve similar goals by optimizing an enzyme's surroundings [1, 4, 16]. This strategy is inspired by metabolic reactions, such as those that make up cellular respiration, where the spatiotemporal efficacy of enzymes is enhanced by its surrounding biological environment [1, 4]. With recent reports highlighting the complex functions of biological condensates *in vivo* (signaling, reaction networks etc.), we took a biomimetic approach in constructing a stable and responsive enzymatic compartment [1-5]. Using *de novo* liquid-liquid phase separated synthetic organelles, these microenvironments may be the bridge to advance how enzymatic power is harnessed industrially.

Complex coacervation, an example of associative liquid-liquid phase separation, describes how oppositely charged polyelectrolytes phase separate into a coacervate phase – a dense, polyelectrolyte-rich phase with potential applications in biomolecular encapsulation – and a dilute phase, the supernatant [1]. Because the coacervate phase compartmentalizes both enzymes and substrates within the same microenvironment, enzymes can perform their catalytic functions with greater spatiotemporal efficacy [1-4]. These *de novo* systems are especially advantageous due to their tuneability by a variety of parameters: pH, charge stoichiometry, ionic strength, mixing order, and others [1, 2]. The use of proteins or other charged biomacromolecules as coacervating macro-ions allows further structural modulation through ionic tagging and supercharging [6, 7, 9].

Complex coacervate systems typically involve binary mixtures of oppositely charged components. To simplify coacervate formation, a net charged enzyme is chosen such that it constitutes one of the electrostatic components for complexation [10, 11]. In particular, the weakly anionic enzyme Glucose Oxidase (GOx) was used in conjunction with four structurally distinct polycations: poly(4-vinyl *N*-methyl pyridinium iodide) (qP4VP), poly(allylamine hydrochloride) (PAH), poly(ethyleneimine) (PEI), and poly(1-vinyl imidazole methyl iodide) (PVI). In sum, we sought to elucidate the effects of mixing order, salt concentration, and finally pH on the phase behavior of four different GOx-polycation systems: GOx-qP4VP, GOx-PAH, GOx-PEI, GOx-PVI.

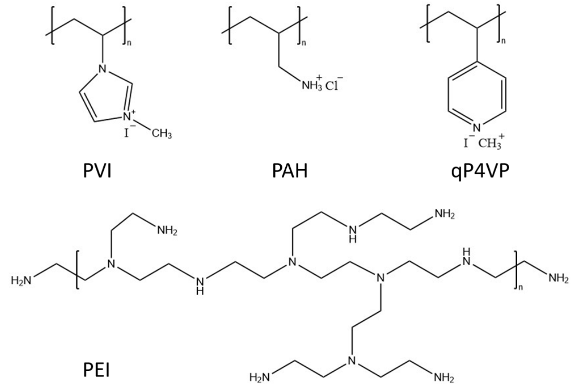

Figure 1. Chemical structures of the four cationic polymers used in this work. Structures were drawn using the ChemDraw Prime software.

METHODS

The phase behavior of four sets of binary GOx-polycation systems were studied. The four sets of polymer-protein mixtures consisted of poly(4-vinyl *N*-methyl pyridinium iodide) (qP4VP), poly(allylamine hydrochloride) (PAH), polyethylenimine (PEI), and poly(1-vinylimidazole methyl iodide) (PVI) as the polycations, with Glucose Oxidase (GOx) as the anionic charged protein. Additionally, we investigated the effects of salt on coacervate formation via the addition of sodium chloride (NaCl). Finally, we utilized pH titrations to explore how complex coacervation can be regulated by solution pH.

Sample Preparation: Glucose Oxidase from Aspergillus Niger was purchased from Sigma Aldrich (G2133). A stock solution of 2 mg/mL GOx was prepared in 10 mM Tris at pH 7.4. Application of Beer's Law was used to determine true concentrations of GOx via its absorbance at 280 nm in a 4 mL quartz cuvette. Polymer solutions were diluted from liquid stocks of 5 mg/mL; relevant stoichiometric calculations using the molar equivalency equation were used to determine the requisite volumes of 10 mM Tris needed to dilute appropriated samples to a mass concentration of 2 mg/mL. Each polycation solution was subsequently adjusted to a pH of 7.4.

Mixing Ratios: Four mixing ratios of GOx/polymer were investigated: 88% GOx/12% polymer, 84% GOx/16% polymer, 80% GOx/20% polymer, 76% GOx/24% polymer. Such values were determined from preliminary data indicating an optimum mixing ratio range for GOx at roughly 80%. Data results for variations in mixing ratios were obtained through turbidimetry analysis and optical microscopy. To exclude external ionic strength contributions in studying mixing ratio effects, salt species were absent in all mixtures.

Salt Effects: The effects of added salt on system phase behavior were examined via turbidimetry analyses and optical microscopy. Sodium chloride (NaCl) concentration was varied from 25 mM to 50 mM on all polymer/protein systems. This salt range was predicted to be conducive for liquid-liquid phase separation in GOx-polymer systems based on preliminary work. For the GOx-PEI system, no form of phase separation was observed at all salt concentrations. Thus, further planned investigations on the GOx-PEI system with salts were abandoned.

pH Titration: The effects of pH on phase behavior reversibility was examined via turbidimetry analysis, based on absorbance readings from an UV-Vis Spectrophotometer, and a pH probe at constant ambient temperature (25 ℃). 1 M Hydrochloric Acid (HCl) was used as the titrant; a 1 cm stirbar at roughly 500 rpm was used to ensure consistent solution mixing throughout the procedure. Each GOx-polycation system was set at its experimentally-determined optimum mixing ratio and salt concentration: 88% mixing ratio, and 50 mM NaCl for all systems with the exception of GOx-PAH, which was set at 175 mM NaCl.

Turbidimetry Analyses: Turbidimetry analyses were done to investigate the effects of mixing ratios and salt concentration. Each sample was prepared in triplicate in tissue culture-treated polystyrene 96-well half-area plates (Corning), followed by incubation at room temperature for 3 h. Using a plate reader (Tecan Infinite M200 Pro), the absorbance of the mixture was taken at a wavelength ($\lambda = 600\ nm$) to monitor scattering of the phase separated mixture. Each sample had an invariant volume of 50 μL allowing for appropriate absorbance measurements and physical mixing by a Tecan Infinite M200 Pro plate reader (10 s of orbital shaking). Finally, the Absorbance was converted into Turbidity using the following set of relationships:

$$\tau = 100 - \%T \tag{1}$$

$$\%T = 10^{(2-A)} \tag{2}$$

Where:

- τ is the Turbidity of the solution and an indicator of the extent of phase separation present within the sample.
- T is the Transmittance of the solution as a function of mixture Absorbance.
- A is the measured Absorbance of the mixture.

Optical Microscopy: All four protein-polymer samples were prepared in triplicate, followed by individual well examination with optical microscopy using an EVOS FL Auto 2 inverted fluorescence microscope (Invitrogen). Each sample, controlled at a volume of 50 μL, were formulated in an optically clear 384-well plate (Nunc) and then underwent 3 h incubation period at room temperature to maximize the degree of liquid-liquid phase separation taking place in the wells (preliminary data indicated that samples tended to favor precipitation following initial mixing before eventual transition into a coacervate phase). All optical microscopy images were taken under 20X objectives with transmitted light.

RESULTS AND DISCUSSION

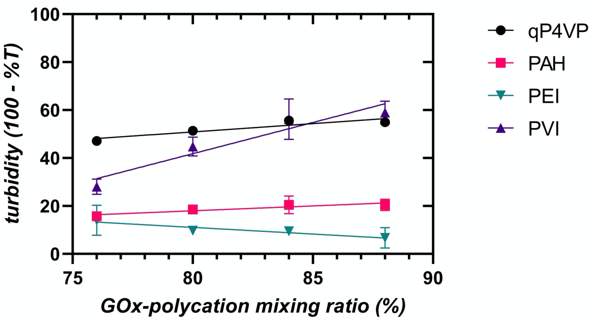

Figure 2. Complex coacervation of Glucose Oxidase (GOx) enzyme with a palette of synthetic polycations. Mixtures were prepared across a select range of macromolecule mixing ratios informed from a more thorough investigation of the protein's phase behavior. Error bars describe the standard deviation of each triplicated data point (n = 3). As a control, all turbidity values shown have had 10 mM Tris turbidity reference values subtracted.

Initial experiments investigated the effects of mixing ratio of protein to polymer using GOx and four different polycations (qP4VP, PAH, PEI, PVI). Preliminary data suggested each binary systems' tendency to phase separate at all four preselected mixing ratios; however, certain mixing ratios resulted in greater extents of phase separation as indicated by their relative turbidity magnitudes. Nevertheless, this initial assumption did not hold as no phase separation was observed with PEI at all mixing ratios. However, we hypothesized that additions of salt may facilitate phase separation through external charge compensations and increasing the total possible conformations of electrostatic associations given the presence of non-polyelectrolyte ions [1, 2, 6]. Thus, PEI was kept for subsequent experiments on the effects of salt addition.

Turbidity data as a function of mixing ratio was plotted in such a way that optimum mixing ratios for each GOx-polycation system can be determined. Although ranging in value from 0 – 100%, turbidity is typically employed as a qualitative indicator in characterizing phase behavior: for example, turbidity values above 20% usually suggest (but do not guarantee) the presence of phase separation whereas values nearing 0% imply the absence of phase separation. However, the presence and exact nature of phase separation, be it liquid-liquid or liquid-solid phase separation, can only be verified through optical microscopy. Nevertheless, turbidity is useful as a continuous measure for when a system exhibits the same morphology under different conditions, and therefore can indicate the conditions most conducive to the desired phase behavior. In this paper, for example, turbidity is used to determine mixing ratios that best drives phase separation. Out of the four mixing ratios investigated, the two mixing ratios most favoring liquid-liquid phase separation will be selected for subsequent investigations involving salt and pH.

It was expected that maximum complexation, as determined by peaks in relative turbidity, for a given GOx-polycation system would lie around mixing ratios of 84% and 88% (although turbidity values were generally higher at a mixing ratio of 92%, optical microscopy showed greater tendencies for precipitation). Indeed, all GOx-polycation systems except for GOx-PEI exhibited coacervate formation at such mixing ratios as determined via optical microscopy (data not shown). Phase separation absence in GOx-PEI also explains the low turbidity magnitudes (below 20% at all mixing ratios). We predicted the absence of phase separation in the GOx-PEI system to be due to the lack of entropic gains from bound counter-ion release in electrostatic interactions within the system as a result of PEI being too weakly charged. The larger relative sample standard deviations with GOx-PVI and GOx-PEI suggests possible systematic inaccuracies: e.g., bubble formation interference at select mixing ratios, but the consistency of turbidity maximums coupled with optical microscopy images (data not shown) at mixing ratios of 84% and 88% supported the selection of these particular mixing ratios for subsequent experiments. While the quantitative limitations of turbidity must be considered, this may also suggest the dominance of (charged) protein-polymers system's electrostatic interactions driving macro-phase separation on turbidity readings as opposed to the strengths of individual components.

Salt Effects

Based on the two selected mixing ratios (88% and 84%) from the previous experimental section, the effects of salt (NaCl) concentration on GOx-polycation phase behavior were investigated (Fig. 3).

Fig. 3c illustrates the characteristic binodal curve phase diagram in phase separating polyelectrolyte systems [1, 8, 12, 14]. In this investigation, however, we are more concerned with determining salt concentrations that promoted liquid-liquid phase separation for the two mixing ratios: 84% and 88%. Turbidimetry analysis was used to provide a relative measure for the degree of phase separation across all GOx-polycation systems and facilitate comparison across the two different salt concentrations. The two chosen salt concentrations were 25 mM and 50 mM based on preliminary data suggesting that this resulted in liquid-liquid phase separation in the GOx-polycation systems being studied.

At both mixing ratios of 84% and 88%, all GOx-polycations that exhibited liquid-liquid phase separation in the absence of salt (Fig. 2) continued to do so with increasing salt concentration. Although GOx-PVI and GOx-qP4VP systems underwent a decrease in turbidity with the addition of salt from 25 mM to 50 mM at constant mixing ratio of 84% (Fig. 3b), optical microscopy still showed liquid-like morphologies. Given that there were still no indicators of phase separation in GOx-PEI with the addition of salt, as suggested by low turbidity magnitudes below 20% (Figs. 3a,

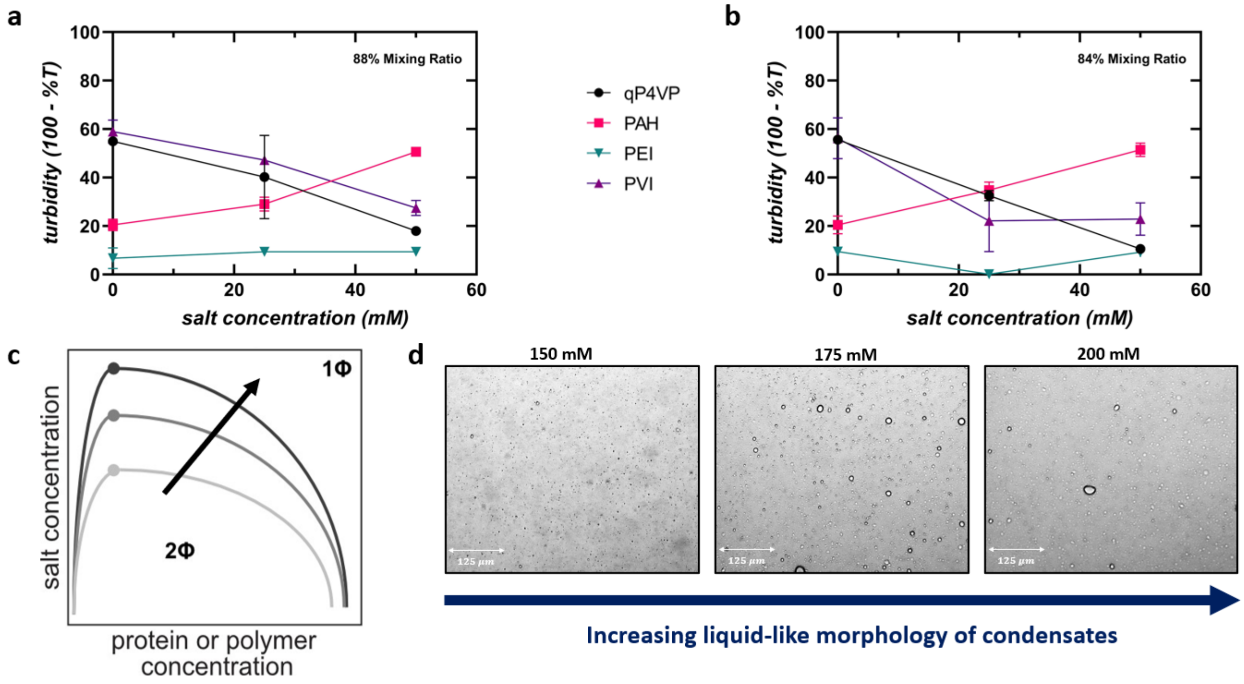

Figure 3. The phase behaviors of multiple GOx-polycation mixtures as functions of salt (NaCl) concentration. GOx-polycation mixtures were prepared using the two optimum mixing ratios for complex coacervation from Fig. 2 (84% and 88%). Both turbidity (λ = 600 nm) and optical microscopy were used to confirm liquid-liquid phase separation. Error bar values represent sample standard deviation; n = 3 for all data points. **a,** Turbidity versus salt concentration at constant mixing ratio of 88%. **b,** Turbidity versus salt concentration at constant mixing ratio of 84%. All turbidity values shown in Figs. 3a and 3b have had 10 mM Tris turbidity reference values subtracted; results from Fig. 2 were also included as no-salt controls. **c,** Binodal phase boundary of complex coacervate systems where both charged polymers and charged proteins facilitate phase separation; Φ denotes 'phase'. Arrow points to increasing two-phase region with increasing macromolecular charge density or patterning, demonstrating phasic tuneability with charge-associated parameters. **d,** Optical microscopy images of GOx-PAH phase behavior (88% mixing ratio) provide sufficient qualitative evidence of liquid-liquid phase separation at salt concentration ranges beyond those in Figs. 3a and 3b.

3b), and confirmed by optical microscopy, the system was excluded from subsequent experiments on the effects of pH on coacervate formation.

As an exception amongst the phase-separating systems, PAH did not demonstrate the desired formation of biomolecular condensates at both salt concentrations of 25 mM and 50 mM based on optical microscopy (data not shown). Instead, its turbidity values consistently above 20% for 25 mM and 50 mM salt concentrations (Figs. 3a, 3b) were shown to be a result of precipitate formation, which furthers evidence for the GOx-PAH system's greater relative propensity for liquid-solid phase separation at the current salt concentration range. For GOx-PAH, low concentrations of salt ions may not provide sufficient charge compensations to favor liquid-liquid phase separation, so much as it is strengthening electrostatic interactions via increasing possible Coulombic-driven conformations. Conversely, at higher salt concentrations, its charge screening effects would work towards dampening such electrostatic interactions to reduce the entropic gains from bound counter-ion release and drive coacervation [2, 6, 12]. An alternative explanation as to the GOx-PAH system's propensity for liquid-solid phase separation at low salt concentrations could be due to kinetic trapping effects as is prevalent in solid phases [2, 8, 12].

Next, experiments with the GOx-PAH system involving higher salt concentrations were necessary to identify a "minimum" salt concentration at which the system undergoes complex coacervation instead of precipitation. Thus, we conducted an additional salt titration exploring GOx-PAH phase behavior at higher salt concentrations: 150 mM to 200 mM NaCl at 25 mM intervals. Samples were analyzed via turbidimetry (data not shown) and optical microscopy (Fig. 3d). While the possibility to utilize a different salt as per the Hofmeister series e.g. KBr was considered, ultimately liquid-liquid phase separation was observed at a NaCl concentration of 150 mM, with the optimum salt concentration for GOx-PAH determined to be 175 mM (Fig. 3d), thereby negating the need to use a different salt species and maintaining consistency across all GOx-polycation systems.

pH Effects

Building on preceding work determining ideal mixing ratio and salt compositions conducive to coacervate formation, the goal of this section is to effectively explore coacervate self-regulation by pH. All GOx-polycation systems were set at an initial pH of ~9.5 in addition to their optimum compositions (specified in the Experimental Section), and a fixed volume of acid was titrated into the solution to slowly decrease the solution pH (Fig. 4b). Reductions in turbidity as pH decreases marks the dissolution of the coacervate microenvironment. Since GOx is characterized as a weak polyelectrolyte and has an isoelectric point (PI) of roughly ~4.2, protonation of GOx below its PI reduces its net negative charge. Thus, the coacervate microenvironment formed by GOx and a polycation would deform as liquid-liquid phase separation dissipates from weakening electrostatic interactions. This is evident from the turbidity of each system being lowest at pH values below 4.2, the isoelectric point of GOx (Fig. 4b). However, the periodicity of the trends, notably with the GOx-PAH and GOx-PVI systems, was unexpected (Fig. 4b). We hypothesize possible induced charging effects on prolonging liquid-liquid phase separation given the uneven anisotropy and charge patchiness of GOx [5, 8]. It is possible the coacervate microenvironment may persist at some of the lower pH ranges due to such effects, which may explain why each system undergoes a transition towards a turbidity maximum at the same pH value of 6 (indicating GOx as the limiting factor) following a local minimum at pH 8~ due to the initial decrease in pH.

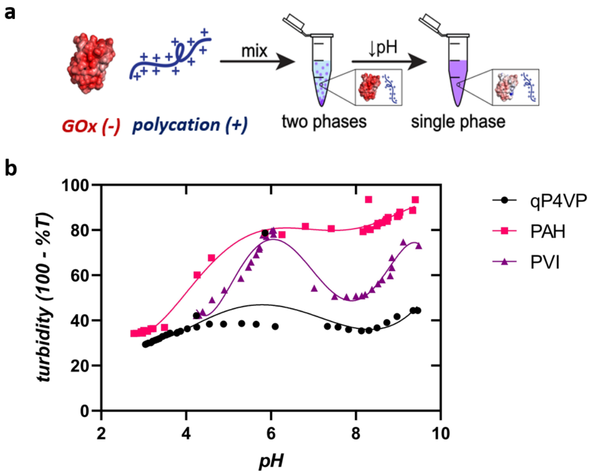

Figure 4. The effects of pH on complex coacervation in multiple GOx-polycation systems. Each GOx-polycation mixture was set at pH of roughly 9.5, followed by titration of hydrochloric acid (HCl) until dissolution of complexation. Turbidity (λ = 600 nm) was used to indicate absence of phase separation upon convergence towards a minimum value after multiple pH titrates. **a,** Schematic depicting pH-induced dissolution of complex coacervation via protonation of GOx, which reduces its net negative charge. **b,** Measured turbidity of GOx-polycation systems as a function of pH. 5th order polynomials were plotted to visualize turbidity trends with pH and to guide the eye (a 5th order polynomial represented the lowest-degree polynomial containing the local extremas that track the data)

Ultimately, we hope to demonstrate pH-mediated regulation of our coacervate microenvironments. Throughout the experimental section, we have shown how coacervate microcompartments can be formed with polymer-enzyme complexes. Further, we can tune the interaction strength and morphology via mixing ratio, salt, and pH. Due to many enzymatic reactions being affected by system pH, demonstrating the microenvironment's ability to form and dissolve reversibly in response to pH represents the primary goal of our work on protein-polymer synthetic nanoreactors [4, 16]. It is important to stress that these results are building blocks towards this objective.

CONCLUSION

An enzyme-polymer complex coacervate system was investigated on the basis of its ability to capture the complexities seen in biological condensates. The phase behaviors of multiple GOx-polycation systems as functions of mixing ratios and ionic strength were investigated. We were interested in each GOx-polycation system's propensity to undergo liquid-liquid phase separation, and the ionic stability of their formed coacervate microenvironments. GOx phase separated upon mixing with the polycations qP4VP, PAH, and PVI; but did not phase separate with PEI. For the GOx-PAH system, the addition of salt was needed to screen existing charge such that the entropic gains favoring liquid-solid phase separation may be suppressed. The GOx-PEI system did not undergo any type of phase separation both with and without the addition of salt. It is also worth remarking that the same species of salt, NaCl, may be used to induce liquid-liquid phase separation for all phase separating GOx-polycation systems, suggesting the salt species' versatility for driving complexation. pH titrations were used to investigate the dynamics of the formed coacervate microenvironments for each GOx-polycation system; turbidimetry suggests that all GOx-polycation systems that phase separated at a pH of ~9.5 no longer phase separated upon reaching pH < PI of GOx. We suggested the possibility of induced-charging effects as an explanation for the periodicity in phase behavior of GOx-PVI as pH decreases, where the anisotropy of GOx and presence of charge patches prolonged phase separation despite non-ideal pH [5, 10, 11]. Nevertheless, while the exact phase behavior of GOx-polycation systems at low pH were not determined as with optical microscopy, due to methodology limitations, the global minimums in turbidity at low pH compared to relative maximums at high pH strongly suggested dissolution of coacervates and dissipation of liquid-liquid phase separation. This crucial finding will inform future work on demonstrating the reversibility of coacervate formation in GOx-polycation systems such that these microenvironments can be made smart and self-regulated to mimic the complexity of condensates found in cells. The establishment of ideal parameters at which various GOx-polycation systems undergo liquid-liquid phase separation provides a foundation for coacervate microenvironment formation for use in advanced synthetic nanoreactor design and elucidation of cellular compartmentalization phenomena.

AUTHOR INFORMATION

Corresponding Author

*htjo@umass.edu

Author Contributions

Hansen Tjo performed the experiments, analyzed data, and produced the figures and the manuscript. Nick Zervoudis devised the experimental plan and reviewed the manuscript. Dr. Allie Obermeyer reviewed the manuscript.

Funding Sources

This work was supported by the Fu Foundation School of Engineering and Applied Sciences at Columbia University and funding from the Columbia Chemical Engineering REU program.

ACKNOWLEDGMENTS

The authors would like to acknowledge members of the Obermeyer Group for helpful discussions.

ABBREVIATIONS

GOx – Glucose Oxidase
HCl – Hydrochloric Acid
NaCl – Sodium Chloride
PAH – Poly(allylamine hydrocholoride)
PEI – Poly(ethylenimine)
PVI – Poly(1-vinyl imidazole methyl iodide)
PI – Isoelectric Point
qP4VP – Poly(4-vinyl N-methyl pyridinium iodide)

REFERENCES

[1] L.P. Bergeron-Sandoval, N. Safaee, S.W. Michnick, Mechanisms and Consequences of Macromolecular Phase Separation. *Cell* **165(5)**,1067–1079 (2016).

[2] W.C. Blocher, S.L. Perry, Complex coacervate-based materials for biomedicine. *Wiley Interdisciplinary Reviews: Nanomedicine and Nanobiotechnology* **9(4)**, doi:10.1002/wnan.1442 (2016).

[3] M. Castellana, M. Z. Wilson, Y. Xu, P. Joshi, I. M. Cristea, J. D. Rabinowitz, Z. Gitai, N. S. Wingreen, Enzyme clustering accelerates processing of intermediates through metabolic channeling. *Nature Biotechnology* **32(10)**, 1011–1018 (2014).

[4] J.-M. Choi, S.-S. Han, H.-S. Kim, Industrial applications of enzyme biocatalysis: Current status and future aspects. *Biotechnology Advances* **33(7)**,1443–1454 (2015).

[5] F. Comert, P.L. Dubin, Liquid-liquid and liquid-solid phase separation in protein-polyelectrolyte systems. *Advances in Colloid and Interface Science* **239**, 213–217 (2017).

[6] C.S. Cummings, A.C. Obermeyer, Phase Separation Behavior of Supercharged Proteins and Polyelectrolytes. *Biochemistry* **57(3)**, 314–323 (2017).

[7] J. Horn, R. A. Kapelner, A.C. Obermeyer, Macro- and Microphase Separated Protein-Polyelectrolyte Complexes: Design Parameters and Current Progress. *Polymers* **11(4)**, 578 (2019).

[8] P. Jha, P. Desai, J. Li, R. Larson, pH and Salt Effects on the Associative Phase Separation of Oppositely Charged Polyelectrolytes. *Polymers* 6(5):1414–1436 (2014).

[9] R. A. Kapelner, A.C. Obermeyer, Ionic polypeptide tags for protein phase separation. *Chemical Science* **10(9)**, 2700–2707 (2019).

[10] L. Li, S. Srivastava, M. Andreev, A.B. Marciel, J. J. D. Pablo, M. Tirrell, Phase Behavior and Salt Partitioning in Polyelectrolyte Complex Coacervates. *Macromolecules* **51(8)**, 2988–2995 (2018).

[11] A.C. Obermeyer, C.E. Mills, X.-H. Dong, R. J. Flores, B.D. Olsen, Complex coacervation of supercharged proteins with polyelectrolytes. *Soft Matter* **12(15)**, 3570–3581 (2016).

[12] S.L. Perry, Phase separation: Bridging polymer physics and biology. *Current Opinion in Colloid & Interface Science* **39**, 86–97 (2019).

[13] S.L. Perry, Y. Li, D. Priftis, L. Leon, M. Tirrell, The Effect of Salt on the Complex Coacervation of Vinyl Polyelectrolytes. *Polymers* **6(6)**, 1756–1772 (2014).

[14] D. Priftis, M. Tirrell, Phase behaviour and complex coacervation of aqueous polypeptide solutions. *Soft Matter* **8(36)**, 9396–9405 (2012).

[15] D. Priftis, N. Laugel, M. Tirrell, Thermodynamic Characterization of Polypeptide Complex Coacervation. *Langmuir* **28(45)**, 15947–15957 (2012).

[16] E. Ricca, B. Brucher, J.H. Schrittwieser, Multi-Enzymatic Cascade Reactions: Overview and Perspectives. *Advanced Synthesis & Catalysis* **353(13)**, 2239–2262 (2011).

CUSJ Article

I’m Upset, not Ashamed: An Investigation into Adolescent Shame Acknowledgement

Olivia Putnam[1]*, Keely Lake[2]

[1]Department of Psychology, Northwestern University, Evanston, IL
[2]Wayland Academy, Beaver Dam, WI

SHAME, EMOTION, PSYCHOLOGY, NEGATIVE AFFECT, MOOD DISORDER, SELF-CONSCIOUS EMOTION

ABSTRACT: Shame is a powerful and acutely painful “master emotion” that is strongly correlated with maladaptive behaviors and a host of psychological symptoms. Concerningly, the affect remains under-researched and difficult to identify or address in a clinical setting. This may be caused, at least in part, by shame’s intrinsically hidden nature, which drives people to deny the emotion and express it through other means. This study aimed to understand the degree to which people fail to acknowledge their own shame and the psychological and behavioral implications of this shame. Participants completed both a self-report measure of shame and an empirical assessment of internalized shame, as well as measures of shame coping methods and emotional regulation. As expected, results showed no significant correlation between participants’ self-rated shame and measured shame. We also saw a significant correlation between assessed internalized shame and use of shame-coping methods as well as difficulty in emotion regulation – specifically, difficulty with clarity of emotion, acceptance of emotions, and strategies for coping with emotions. These findings indicate that people struggle to acknowledge their own shame and also speak to the maladaptive, dysregulated ways people manage their shame. Recognizing shame as a powerful emotion with implications in psychiatric disorders and understanding the factors that prevent people from acknowledging their own shame may help improve treatment for those who struggle with the emotion and reduce the likelihood that they will engage in maladaptive coping behaviors.

INTRODUCTION

Shame is one of the most under-researched emotions. Whereas emotions like sadness, anger, and nervousness have undergone decades of psychological research and have come to be seen as the underlying feelings behind widespread clinical diagnoses like Anxiety or Depression, shame research within the field of psychology was virtually nonexistent until the last two decades and remains remarkably limited today. This lack of research is particularly troubling when it comes to shame because the affect is highly maladaptive. Unsurprisingly, as a result, it is highly correlated with addiction, depression, violence, aggression, bullying, suicide, and eating disorders. In recent years, it has also become an emerging component of PTSD (Taylor, 2015).

A Brief History of Shame Conceptualization

One especially influential early premise for defining shame, and differentiating it from guilt, is early anthropologists’ focus on public vs. private transgressions (e.g., Benedict, 1946). Anthropologists commonly distinguished shame based on the situations they believed elicited it. More specifically, shame was conceived as a "public" emotion, arising from public exposure and disapproval of some transgression in societal rules and norms. Guilt, on the other hand, was described as a more "private" experience arising from self-inflicted criticism and regret. However, more recent empirical research has failed to support this public/private distinction (Tangney, Marschall, Rosenberg, Barlow & Wagner, 1994; Tangney, Miller, Flicker & Barlow, 1996). One such example is a study conducted in 1992 asking participants to describe three guilt-inducing events and three shame-inducing events. A systematic analysis of the social context of these events found that shame and guilt are equally likely to be experienced in the presence of others (Tangney, et al., 1992). "Solitary" shame experiences were equally as common as "solitary" guilt experiences. Even more to the point, “the frequency with which others were *aware* of the respondents' behavior did not vary as a function of shame and guilt” (Tracy, 2011).

This led to a new conceptualization of shame which remains today: shame as holistic negative self-concept. Helen Block Lewis, renowned psychologist and pioneer of this shame-understanding, asserted that while guilt involves a negative evaluation of a specific behavior, shame involves a negative evaluation of the global self ("I did something bad" vs. "I am bad") (1971).

Though the distinction may appear inconsequential, this contrasting emphasis on the self “sets the stage for very different emotional experiences and very different patterns of motivation `and subsequent behavior” (Tracy, 2011). The two emotions, for instance, produce distinct "action tendencies." Shame is commonly accompanied by attempts to deny, hide from, or escape the experiences that elicit shame, while guilt typically leads to "reparative action" – confessing, apologizing, undoing.

This difference in internal conceptualization of the self and subsequent "action tendencies" is part of what ultimately makes shame maladaptive. While guilt can be painful and overwhelming, it is generally limited to the guilt-inducing action or experience. Shame consumes the entire self, leaving experiencers with a globally-negative self-conception ("I am a terrible person"). This negative self-concept is not only painful and distressing, but it also feels irreparable. A person can correct a behavior, but one's fundamental essence seems permanent. This sense of futility drives much of shame's maladaptivity. Rather than embracing adaptive behaviors like apologies or changes in behavior, which increase psychosocial success, shame-experiencers tend to recede and hide from the shame-inducing event. Often, this leads people to isolate themselves socially, withdraw from activities that potentially remind them of the shame, and engage in anhedonic-behaviors. In other cases, this avoidance manifests as anger or hostility, as experiencers attempt to "turn the tables" on others to avoid their own shame, or as risky behavior (i.e. substance abuse) which many use a distraction from their shame (Ellison, 2006).

In instances where shame-experiencers have in fact committed some wrongdoing (the determination of which is of course subjective) the failure to take the expected "reparative action" can lead to social conflict (Tangney, Stuewig & Mashek, 2007). For those who experience shame about events for which reparative action is not typically expected (i.e. being the victim of sexual assault, mental illness, minor mistakes or failures), shame can cause dissociation, debilitate people from talking about their experience, and limit much-needed processing of their own emotions and/or trauma (Taylor, 2015). Either way, these maladaptive responses to shame led researchers to "consistently report a positive relationship between proneness to shame and a host of psychological symptoms, including depression, generalized anxiety and social anxiety, low self-esteem, PTSD, eating disorder symptoms, Cluster C personality disorders, suicidal behavior and self-injurious behavior, and substance abuse" (Tracy, 2011).

Shame Acknowledgement

In the context of shame's maladaptive consequences, the lack of research into the affect becomes dangerous. Without comprehensive research into shame and its implications in psychological disorders, we cannot develop evidence-based treatments for shame-related disorders or, more importantly, adjust treatments for preexisting mental health disorders in which shame plays a more important role than previously-realized.

One roadblock that commonly hinders the development of these treatments or the confrontation of shame within a therapy setting is the fact that shame often goes unacknowledged by the experiencer (McGonigal, 2016). As Terry F. Taylor Ph.D. writes in a review article of peritraumatic shame, "Shame...is a virtually invisible, ubiquitous part of everyday life. Because the experience of shame is often considered to be painful and disempowering, and because recognition of shame in itself can be felt as shameful… shame remains unacknowledged and is expressed as avoidant behavior" (2015). This instinct to hide one's shame "makes it difficult to recognize internally when it happens," let alone acknowledge out loud (Luoma, 2012). Concerningly, this tendency among people not to acknowledge their own shame also makes it difficult to study the affect, as it renders self-report measures unreliable.

Present Study

The consensus that shame characteristically goes unrecognized has never been scientifically reviewed. Further, researchers have not studied whether the degree to which people report their own shame correlates with their mental health in other capacities. Our research attempts to fill this gap. Like most shame-studies before it, we utilize assessments intended to empirically measure participants' levels of shame. In addition to these assessments, however, we also use an assessment of emotional affect that asks participants to self-rate the frequency with which they experience different emotions, "ashamed" being one them. Comparisons of participants' scores on the shame assessments and their self-reported level of shame will act as quantified measurements of how well they acknowledge their own shame.

This research will not only test the assumption of shame's unidentified nature but may also provide some insight into the prevalence of unacknowledged shame and how it affects people's mental health.

METHODS

Participants and Procedure

The assessments were administered to a sample of 54 adolescent students between the ages of 14 and 17 (58% female, 42% male, $M = 16.3$ years old, $SD = 1.3$, 55% American). Participants were recruited from the student population at Wayland Academy, a small boarding high school with international students. As an incentive for participation, students were offered a small amount of extra credit in their science and math classes. Participants were each given a battery of psychological assessments including the Positive and Negative Affect Scale (PANAS), the Internalized Shame Scale (ISS), the Compass of Shame Scale (CSS), and the Difficulty in Emotion Regulation Scale (DERS). Participants were assured that their responses would be anonymous and confidential. Assessments were given in a quiet, distraction free room.

Assessments

Positive and Negative Affect Scale: (PANAS; Watson and Clarke, 1998) The most commonly used measure of affect in scholarly research, the PANAS is comprised of 10 negative affects (afraid, upset, distressed, jittery, nervous, ashamed, guilty, irritable, hostile) and 10 positive affects (enthusiastic, interested, determined, excited, inspired, alert, active, strong, proud, attentive). Participants use a 0-4 Likert scale to rate the frequency with which they tend to experience each affect. For the purposes of this research, the "ashamed" item was used to measure self-rated shame because, unlike empirical assessments of shame, it requires participants to explicitly endorse the word "ashamed."

Internalized Shame Scale: (ISS; Rosario and White, 2006) The Internalized Shame Scale, a 30-item questionnaire, is the most widely used empirical measure of shame across psychology and sociology research. The assessment has two subscales that are intended to be reported separately: a 24-item shame scale and a 6-item self-esteem scale. The shame scale attempts to tease apart different experiences of shame to create a holistic measure of the affect. Importantly, the ISS does not actually use the word shame, because shame can itself be a shameful thing to admit. There are four identified cutoffs: a score of 50 or higher indicates problematic levels of shame, a score of 60 or higher indicates possible depression and/or other emotional or behavioral problems, a score of 70 or higher indicates a high probability of depression and/or other emotional or behavioral problems.

Compass of Shame Scale: (CSS; Ellison, 2006) Because shame is an emotion that commonly goes unacknowledged both internally and outwardly, it is often expressed through other emotions or behaviors. The Compass of Shame Scale recognizes this tendency and assesses the maladaptive ways people cope with shame. The four coping methods that it identifies are "Attack Self," "Attack Others," "Withdraw," and "Avoid." This scale is of particular importance because it acknowledges shame as a fundamental source for many other maladaptive, unhealthy behaviors and is the first of its kind to assess and quantify these shame-based behaviors. Additionally, the test questions are situational rather than experiential. Participants cannot always recognize feelings as shame, but they can often identify situations that produce those shame feelings.

Difficulty in Emotional Regulation Scale: (Gratz, 2004) This assessment represents one of the most popular, comprehensive and well-established measures of emotion regulation and is widely used in both clinical and nonclinical settings. The questionnaire assesses five primary components of emotional regulation: emotional awareness, emotional clarity, emotional acceptance, impulse control, ability to engage in goal-directed behavior while experiencing negative emotions, and ability to use situationally appropriate emotion regulation strategies flexibly to modulate emotional responses as desired.

RESULTS

Self-Rated Shame vs. Measured Shame

To investigate the relationship between self-rated shame and measured shame, Pearson correlations were computed between ratings from the PANAS item "ashamed" and scores from the Internalized Shame Scale. As expected, there was no significant correlation between self-rated shame and assessed "true" shame. The correlation and significance are displayed in Figure 1.

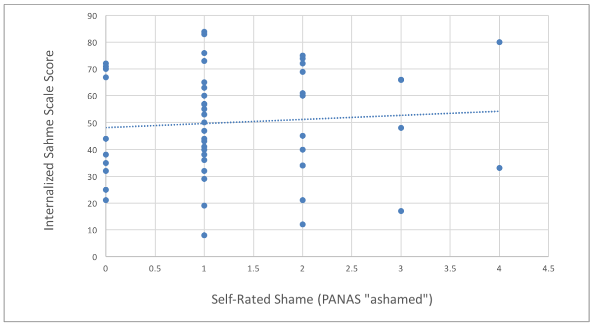

Figure 1. Pearson correlation between PANAS "ashamed" score and Internalized Shame Score. This graph shows the Pearson correlation between PANAS "ashamed" rating and ISS scores, r = 0.0806, p > 0.05

To visualize how shame acknowledgment relates to shame's maladaptivity, an ANOVA test for the significance of differences in mean PANAS "ashamed" ratings among internalized shame cutoff groups – shame w/in normal limits, problematic levels of shame, possible indicator of mental health disorders, and likely indicator of depression/mental health disorder -- was performed and is displayed in Figure 2.

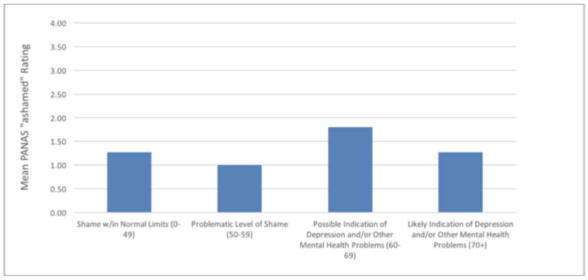

Figure 2. Analysis of Variance test of PANAS "ashamed" score by ISS cutoff groups. This graph shows the mean PANAS ashamed ratings reported by individuals in different ISS cutoff groups, f ratio = 0.903, p > 0.05

As expected, and in line with our other findings, there was no significant difference in self-rated shame (PANAS "ashamed") between among ISS cutoff groupings (i.e. all participants reported similar levels of sham, no matter how much shame an individual was actually experiencing).

Identifying Shame as Negative Affect

In order to explore whether participants may identify their internalized shame as other negative emotions, Pearson correlations were computed between PANAS Negative Affect item scores and Internalized Shame scale scores. Both are displayed in table 1.

Table 1. Pearson correlations between PANAS negative affect subscores and Internalized Shame Scale score. This table shows the results of Pearson correlations between various PANAS negative affect subscores and ISS score.

Negative Affect	***beta-co* (r)**	***sig* (p)**
Distressed	0.451	0.000
Upset	0.215	0.122
Guilty	0.318	0.021
Scared	0.266	0.114
Hostile	0.217	0.012
Irritable	0.342	0.012
Ashamed	0.081	0.564
Nervous	0.393	0.004
Jittery	0.24	0.083
Afraid	0.380	0.005

There was also a significant positive correlation between PANAS Negative Affect Subscale total score and Internalized Shame score (r = 0.534, $p < 0.01$).

Implications of Shame

To investigate shame's relationship with other emotional and behavioral problems, Pearson correlations were computed between ISS scores and scores on the individual Compass of Shame scales and the Difficulty in Emotion Regulation Scale (Figure 3).

Strong correlations between the ISS and the Withdrawal and Attack Self scales were expected and obtained. Both correlations were significantly stronger than the ISS correlations with the Avoidance and Attack Other scales. All correlations were significant.

Category Differences

Male/Female, Age, and Continent of Origin differences were assessed for both the Internalized Shame Scale and the PANAS "ashamed" rating. Women tended to have higher Internalized Shame scores than men (t = 1.76, $p < 0.05$). There was no significant difference, however, between men and women for the PANAS "ashamed" rating. There was also no significant correlation between age and Internalized Shame Score or the PANAS "ashamed" rating. Continent of origin did not produce any significant differences in ISS score or PANAS "ashamed."

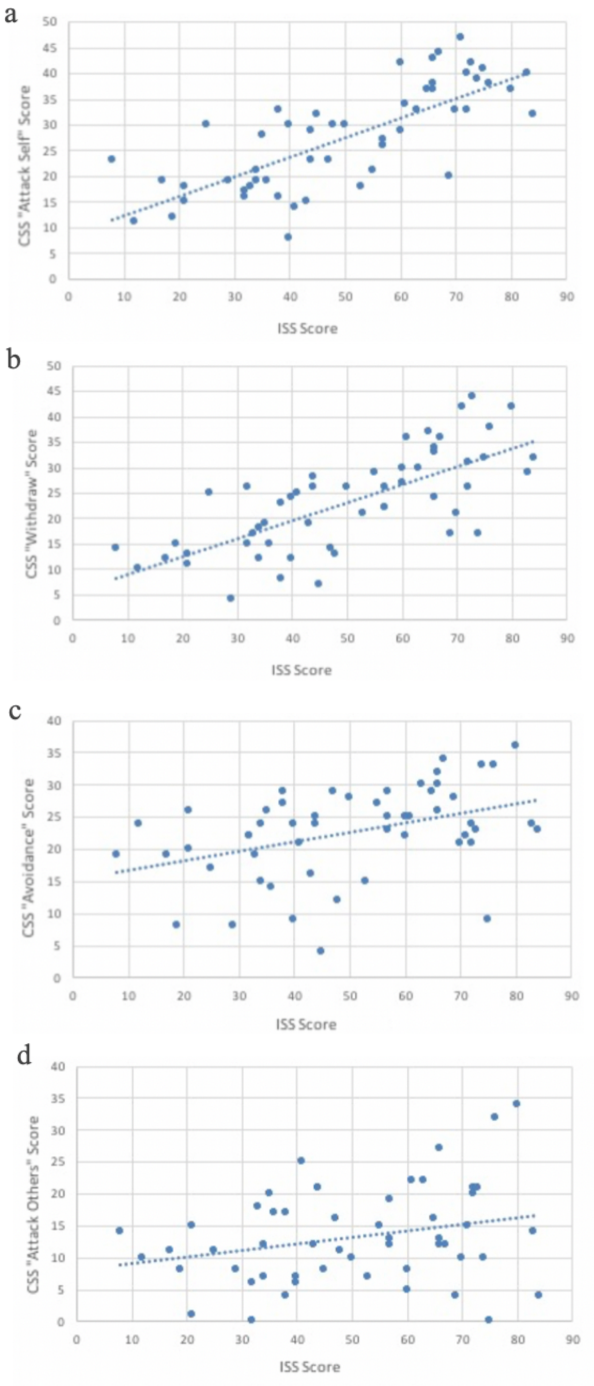

Figure 3. Pearson correlations between CSS subscores and ISS Scores. **a,** Pearson correlation between CSS attack self subscore and ISS score, r = 0 .75, $p < 0.001$ **b,** Pearson correlation between CSS withdraw subscore and ISS score, r = 0 .72, $p < 0.001$ **c,** Pearson correlation between CSS avoidance subscore and ISS score, r = 0.41, $p < 0.01$ **d,** Pearson correlation between CSS attack others subscore and ISS score, r = 0.27, $p < 0.05$

DISCUSSION

The lack of correlation between ISS score and PANAS "ashamed" rating, as displayed in Figure 1, indicates that there is no relationship between self-rated shame and empirically-measured "true" shame. This is further demonstrated by the analysis of variance displayed in Figure 2, which shows that there is no significant difference in self-rated shame between cutoff categories of "true" ISS shame. Essentially, even those who experience shame at an intensity high enough to indicate depression or other mental health disorders tended to describe their experience of shame as "rare." A paired t-test comparing average ISS shame and PANAS shame affirmed this underreporting phenomenon in individuals, with nearly 74 percent of participants reporting lower self-rated PANAS shame than "true" ISS shame.

Importantly, there was a significant positive correlation between ISS score and PANAS Negative Affect subscale score, suggesting that while people struggle to accurately identify their shame, they may describe it broadly as negative affect. This point is reiterated by the fact that, with the exception of "distressed," the individual PANAS negative affect items had weak or insignificant correlations with ISS score and none had stronger correlations than the Negative Affect subscale score. This indicates that people are not calling shame by another name, but instead use negative umbrella terms, or a variety of different emotion words, to imprecisely describe the feeling. These results both confirm a common understanding that shame often goes unacknowledged and also underline the difficulty of identifying and properly addressing shame.

This pattern becomes especially meaningful in the context of internalized shame's negative implications. ISS score was found to have positive correlations with all CSS scales: attack self, withdraw, avoid, and attack others. Given their naturally internalized nature, the "withdraw" and "attack self" coping mechanisms had a stronger relationship with internalized shame than "avoid" or "attack other." Internalized shame also showed a strong positive relationship with DERS score and with the lack-of-clarity, non-acceptance, and strategies subscales specifically. This fits well with the findings about unacknowledged shame, as clarity and acceptance are both components of emotional acknowledgment, and are necessary for strategic management of one's emotions.

The male/female differences on the ISS reflect those of previous studies, with women tending to experience more internalized shame than men. Also similar to adult studies, age was not a significant factor in ISS score, suggesting that experience of shame does not change significantly during adolescent development. Given that this comes from a cross-sectional review rather than a longitudinal one, however, the accuracy of this conclusion is limited. Continent of origin, which has never before been studied in relationship to internalized shame, produced no significant difference. The accuracy of this conclusion, however, may be compromised by the small and varying number of participants within each continent group.

CONCLUSION

The comparisons of self-rated shame and empirically measured "real" shame confirm both our hypothesis and a larger long-held public understanding that people hesitate to acknowledge their shame. This finding is important not only because it is the first of its kind to quantitatively validate that informal understanding, but, more significantly, because it speaks to the extent of the disparity. More than one third of participants experienced internalized-shame with a frequency associated with depression and other clinical disorders, yet the great majority of these participants rated their own experience of shame as rare. This is problematic because, if people cannot acknowledge shame as a component of their emotional distress or mental illness, then these problems become much more difficult to address within a clinical or intrapersonal context. This lack of acknowledgment becomes especially concerning if the shame centers around a specific, potentially-traumatic event (i.e. sexual assault). If shame prevents a person from speaking up about and working through such an experience, then symptoms can worsen dramatically. As time goes on, this can also become a self-fulfilling prophecy of sorts because the longer one avoids their shame the more internalized it becomes and, consequently, the more inhibiting it becomes.

Given that shame is a powerful emotion, however, it cannot be entirely ignored or suppressed. In fact, this study's findings indicate that people may be able to recognize the emotion broadly as emotional distress. However, without specific identification and management, shame is often expressed through maladaptive coping mechanisms. The correlation between internalized shame and each pole of the shame-coping scale suggests that, rather than addressing shame head on, shame-experiencers tend to avoid the emotion through problematic behaviors such as: risk-taking and distraction, which can develop into substance abuse and have been shown to be severely maladaptive; withdrawal from social interaction, often a symptom of depression; excessive self-criticism, also related to mental illness; or attacking others, an instinct associated with aggression and potential violence. Though they vary in commonality, each pole is maladaptive in its own right—an attempt to ignore, hide from, wallow in, or push back one's shame without ever truly acknowledging it. It is also important to note that these individuals coping mechanisms are not orthogonal and in fact tend to converge.

This tendency to cope with shame is similarly reflected by the significant correlation between internalized shame and difficulty in emotional regulation. Even more to the point, the DERS subscales that had the strongest relationships with shame were lack-of-clarity, non-acceptance, and strategies. This indicates that people with high levels of internalized shame have significant trouble identifying their emotions, acknowledging their emotions without guilt or embarrassment, and coping with their emotions effectively. This not only speaks to the troubling ways people manage their shame but also to the dysregulatory nature of shame itself, which can make it more difficult for a person to manage any of their emotions.

The implication of these findings is three-fold: tools for shame recognition must be better integrated into both clinical and intrapersonal settings, shame must be better accounted for within diagnostic criteria, and more research into the affect must be conducted. It is imperative that mental health practitioners recognize that patients are unlikely to forthrightly acknowledge or report their shame and that these practitioners are trained in how to identify this underlying shame and address it without causing the patient to shut down or react with anger. It is also an unfortunate truth that, because the perception of shame in others "can also evoke a discomforting emotion in the observer," it may fail to be addressed in therapy, with the therapist remaining in an "unconscious collusion with the patient" to ignore the shame (Taylor, 2015). Additional shame-specific training and wider acknowledgement of the emotion's role in psychopathology may help mediate this problem

An important step in helping clinicians (and, in fact, any individual) better identify and work with shame is better accounting for the emotion in diagnostic criteria. Despite the fact that the emotion is strongly correlated with many different mental illnesses and social-emotional problems, shame is rarely listed as a symptom in the DSM IV and is generally relegated to the "associated features" of a disorder. Not only does this lack of representation reinforce shame's hidden nature, but it also fails to account for the way shame's role in a disorder can change the way it must be treated.

Perhaps most importantly, more scientific research must be conducted into shame. Since shame's psychological conceptualization as holistic self-blame was established, only a handful of scientific studies into the affect have been conducted and, even fewer yet have investigated shame's role in psychiatric disorders. If we are to help people recognize and cope with their internalized shame, we must first understand what prevents that acknowledgment and which tools are the most effective in fostering it.

AUTHOR INFORMATION

Department of Psychology, Northwestern University
Evanston, IL, USA

REFERENCES

[1] H. L. Bash, A. Papa, Shame and PTSD symptoms. *Psychological Trauma: Theory, Research, Practice, and Policy.* **6(2)**, 159–166 (2014).

[2] R. Benedict, The Chrysanthemum and the Sword, (Houghton Mifflin Harcourt, 1946).

[3] P. M. Del Rosario, R. M. White, The Internalized Shame Scale: Temporal stability, internal consistency, and principal components analysis. *Personality and Individual Differences.* **41(1)**, 95–103 (2006).

[4] J. Elison, R. Lennon, S. Pulos, Investigating The Compass Of Shame: The Development Of The Compass Of Shame Scale. *Social Behavior and Personality: an international journal.* **34(3)**, 221–238 (2006).

[5] K. L. Gratz, L. Roemer, Multidimensional Assessment of Emotion Regulation and Dysregulation: Development, Factor Structure, and Initial Validation of the Difficulties in Emotion Regulation Scale. *Journal of Psychopathology and Behavioral Assessment.* **26(1)**, 41–54 (2004).

[6] H. B. Lewis, Shame and guilt in neurosis, (International Universities Press, 1974).

[7] J. Luoma, J. LeJeune, Association for Contextual Behavioral Science. (2005). Available at: https://contextualscience.org/acbs

[8] K. McGonnigal, R. D. Siegel, Breaking the Power of Shame by Engaging it. (2016). Available at: https://nextlevelpractitioner.nicabm.co/week40/

[9] L. A. Medrano, M. Trogolo, Construct Validity of the Difficulties in Emotion Regulation Scale: Further Evidence Using Confirmatory Factor Analytic Approach. *Abnormal and Behavioural Psychology.* **2(2)**, 1000117 (2016).

[10] P. Michl, et al, Neurobiological underpinnings of shame and guilt: a pilot fMRI study. *Social Cognitive and Affective Neuroscience.* **9(2)**, 150–157 (2012).

[11] D. Sznycer, et al, Cross-Cultural Differences and Similarities in Proneness to Shame: An Adaptationist and Ecological Approach. *Evolutionary Psychology.* **10(2)**, 147470491201000 (2012).

[12] K. Tangey, W. Fischer, Self-conscious emotions: Shame, guilt, embarrassment, and pride, (Guilford Press, 1995).

[13] J. P. Tangney, Recent Advances in the Empirical Study of Shame and Guilt. *American Behavioral Scientist.* **38(8)**, 1132–1145 (1995).

[14] J. P. Tangey, "Shame and guilt in interpersonal relationships" in Self-Conscious Emotions: The Psychology of Shame, Guilt, Embarrassment, and Pride, J. P. Tangey, K. W. Fisher, Eds. (Guilford Press, 1995), pp 114-139.

[15] J. P. Tangney, Conceptual and methodological issues in the assessment of shame and guilt. *Behavior Research and Therapy*. **34(9)**, 741-754 (1996).

[16] J. P. Tangney, S. A. Burggraf, P. E. Wagner, "Shame-proneness, guilt-proneness, and psychological symptoms" in Self-Conscious Emotions: The Psychology of Shame, Guilt, Embarrassment, and

Pride, J. P. Tangey, K. W. Fisher, Eds. (Guilford Press, 1995), pp. 343-367.

[17] G. Taylor, Pride, Shame and Guilt: Emotions of Self-Assessment. *Philosophical Books.* **28(1)**, 40–41 (1987).

[18] T. F. Taylor, The influence of shame on posttrauma disorders: have we failed to see the obvious? *European Journal of Psychotraumatology.* **6(1)**, 28847 (2015).

[19] J. Tracy, J. P. Tangney, M. R. Leary, Handbook of self and identity, (Guilford Press, 2012).

[20] D. Watson, L. A. Clark, A. Tellegen, Development and validation of brief measures of positive and negative affect: The PANAS scales. *Journal of Personality and Social Psychology.* **54(6)**, 1063–1070 (1988).

[21] M. R. Zaslav, Shame-Related States of Mind in Psychotherapy. *J Psychother Prac Res.* **7(2)**, 154–166 (1998).